Polarized Radiative Transfer Modeling: An Application to Microwave Remote Sensing of Precipitation

By
K. Franklin Evans and Graeme L. Stephens

Department of Atmospheric Science
Colorado State University
Fort Collins, Colorado

Colorado
State
University

Department of
Atmospheric Science

Paper No. 461

POLARIZED RADIATIVE TRANSFER MODELING: AN APPLICATION TO MICROWAVE REMOTE SENSING OF PRECIPITATION

K. Franklin Evans and Graeme L. Stephens

Department of Atmospheric Science

Colorado State University

Fort Collins, CO 80523

of the precipitation–microwave function. The fraction of pairs of output vectors that were closer than a specified distance was computed, and statistics were accumulated on the differences between the corresponding atmospheric states of these pairs. The relative importance of various sets of frequencies for precipitation retrieval was determined by performing the analysis for different combinations of frequencies. The analysis showed that low frequencies ($\leq$ 10 GHz) are crucial for accurate precipitation retrieval, and that, over both land and water surfaces, several frequencies (four or more) are required for a retrieval to be reasonably unique.

ACKNOWLEDGEMENTS

CONTENTS

LIST OF FIGURES

LIST OF TABLES

Chapter 1

INTRODUCTION

1.1 The Importance of Precipitation Measurements to Climate

Besides being of critical importance to the well-being of mankind the distribution of precipitation across the globe is a major element of the climate system. The latent heat release associated with areas of precipitation in the Intertropical Convergence Zone (ITCZ) is a main driving force of the low-latitude circulation of the atmosphere. Precipitation is both an important climate element in its own right and a physical process of great significance to the general circulation of the atmosphere. An accurate global climatology of precipitation is important for verifying general circulation models (GCMs). The physical processes leading to precipitation are below the grid resolution of GCMs, and semi-empirical parameterization schemes must be used to predict clouds and precipitation. The parameterizations in GCMs are currently rather crude, and detailed global precipitation data will be needed to make improvements in climate modeling.

Of the processes making up the hydrological cycle (evaporation, water vapor transport, and precipitation), precipitation is, perhaps, the least understood. The detailed global distribution of precipitation amounts and variabilities is inadequately known. Rainfall is spatially highly variable and point measurements, such as rain gauges, provide poor estimates of area averaged rainfall even in regions with networks of gauges (Thiele 1987). In sparsely inhabited regions and over the oceans rain gauge data are nearly non-existent. Well calibrated radars, especially polarization capable ones, accurately measure rainfall over an area, but the coverage is limited to areas with radar networks. Satellite remote sensing offers the most practical way of obtaining the global distribution of precipitation. Rainfall retrieval algorithms based on geosynchronous IR data have been proposed

(Arkin 1979), but these methods are rather indirect and inaccurate. The Tropical Rainfall Measuring Mission (TRMM) (Simpson et al.,1988) is being planned to measure a rainfall climatology of the tropics during the mid-1990's. The low-earth orbit satellite will carry 19, 37, and 85 GHz passive microwave scanning radiometers, single frequency microwave radar, and visible and infrared radiometers. The TRMM passive microwave rainfall retrieval algorithm, however, has not yet been developed.

1.2 Passive Microwave Remote Sensing of Precipitation

Microwave wavelengths are suitable for the remote sensing of precipitation because the radiation interacts strongly with hydrometeors, which have sizes of the same order as microwaves. Microwaves penetrate through non-precipitating clouds with little attenuation, whereas visible and infrared radiation are attenuated over relatively short distances. Raindrops absorb, and correspondingly emit, microwave radiation. Large raindrops also significantly scatter the higher frequency microwaves (>50 GHz). Precipitation sized ice particles, on the other hand, absorb very little and so interact with microwaves primarily through scattering. In general the higher the frequency the more attenuation, by absorption or scattering, the microwaves suffer. What these properties mean for remote sensing of precipitation depends on the circumstances. Over a water surface, which has a low emissivity and is thus radiometrically "cold", the emission from raindrops increases the microwave signal (increases the "brightness temperature"). As the rain layer thickens or the rainfall rate increases the attenuation increases and the increase in signal tapers off. This saturation occurs with lower rainfall rates at higher microwave frequencies. Unlike land surfaces, the emission from water surfaces is highly polarized, with the vertical component larger than the horizontal one. Along with warming the brightness temperature over water, rain and clouds also reduce the degree of polarization. Over land, which usually has an emissivity near one, raindrops lower the brightness temperature very slightly because they are somewhat cooler than the surface. Convective rainfall is usually accompanied by significant amounts of large ice particles above the rain. The ice scatters the upwelling radiation away, and doesn't emit much to replace it, and so can greatly lower the

observed brightness temperature. This decrease in the microwave signal is especially large at high frequencies (85 GHz and above). The brightness temperature lowering due to ice particles occurs independent of the type of surface, but the ice is not directly related to the amount of precipitation reaching the ground. Along with the effects mentioned above, the rain or ice particle size distributions, particle shapes, cloud droplet mass, water vapor, temperature, surface emissivity, and vertical and horizontal inhomogeneities all affect the upwelling microwave radiation from a precipitating atmosphere.

Since the early 1970's investigators have been using passive microwave radiometer data from earth orbiting satellites to infer information about precipitation (Njoku 1982). The 19 GHz ESMR (Electronically Scanned Microwave Radiometer) was launched on Nimbus-5 in 1972. Wilheit et al. (1977) used the ESMR data to sense rainfall over the ocean. A radiative transfer model with a simple precipitation structure retrieved the rainfall rate with an accuracy of about a factor of two. Microwave observations from space took a large step forward in 1978 with the SMMR (Scanning Multichannel Microwave Radiometer) instrument on Nimbus-7 and Seasat. SMMR had horizontally and vertically polarized channels at 6, 10, 18, 21, and 37 GHz. Work by Spencer et al. (1983) is an example of rainfall retrieval from SMMR data. They used multiple regression to relate the brightness temperatures of seven microwave channels (10 to 37 GHZ) to weather radar derived rain rates. The newest satellite microwave sensor is the SSM/I (Special Sensor Microwave/Imager) which was launched in 1987. This instrument has both polarizations at 19, 37, and 85 GHz and vertical polarization at 22 GHz. SSM/I has greater sensitivity than SMMR, and higher resolution at 85 GHz (15 km). Spencer et al. (1989) used the two channels at 85 GHz to define a precipitation indicator that uses the depolarization from precipitation to overcome the ambiguity of interpreting low brightness temperatures arising from low emissivity surfaces or scattering by ice.

Observational studies either have not attempted to retrieve rainfall rates or have large uncertainties in the retrievals. Some of the errors are due to problems with ground truth accuracy and with inadequate horizontal resolution of the instruments. Given the many atmospheric variables that affect upwelling microwave radiation, however, it is to

be expected that precipitation retrieval would be difficult. Recent theoretical radiative transfer modeling (described in chapter 5) suggests that multiple frequencies could be used to improve the accuracy of rainfall retrieval. The most accurate microwave rainfall retrieval scheme currently proposed (Kummerow et al. 1989) uses this multi-frequency approach in a physical (i.e. radiative transfer based) method. The hypothesis that multiple frequencies will make precipitation retrieval accurate, leads to the question of how many and which frequencies are needed. And more fundamentally, is the precipitation–microwave radiance function invertible at all; will *any* number of frequencies be enough?

1.3 Scientific Objectives

This work is a part of the long term effort toward accurate remote sensing of precipitation from space-based platforms. The goals of this work are to develop a radiative transfer model that could be used by the microwave remote sensing community, and to add to the understanding of microwave radiative transfer in precipitation.

The specific objectives of this research are:

1. To develop a monochromatic polarized plane-parallel radiative transfer model for general purpose use in remote sensing. The model should be highly accurate (within the plane-parallel constraint) and treat polarization fully and correctly. It should be relatively simple, maintainable, reliable, and well tested.

2. To determine to what degree such a radiative transfer model is an improvement over simple models in microwave radiative transfer. The microwave brightness temperatures upwelling from simple precipitating atmospheres are calculated and compared between the model developed here and an Eddington-type two-stream model.

3. To use the radiative transfer model to study the question of invertibility of the precipitation–microwave brightness temperature function. The relative importance of various frequencies and of polarization is determined.

1.4 Plan of This Research

A detailed description of the radiative transfer model developed for this work is described in chapters 2 and 3. Chapter 2 describes the microwave absorption and scattering methods. The general purpose radiative transfer model is described in chapter 3. This chapter presents the mathematics of the algorithm, while the appendices describe some new numerical quadrature schemes and give an outline of the radiative transfer algorithm. Chapter 4 develops the simple Eddington-type model and compares the output of the two models for simple precipitation structures. Chapter 5 presents the precipitation invertibility study. The radiative transfer modeling and the unique analysis of the model output is described. The issue of invertibility in microwave precipitation retrieval has not been previously studied in the systematic way done here. Chapter 6 summarizes the model and results and presents conclusions.

Chapter 2

MICROWAVE ABSORPTION AND SCATTERING

Computing the upwelling microwave radiation from a precipitating atmosphere naturally divides into two steps: calculating the constants in the radiative transfer equation (which are the properties of the medium), and solving the radiative transfer equation. The first step, described in this chapter, is computing the absorption by gases and cloud droplets and computing the single scattering properties of raindrops and ice particles. For this research the scattering particles are assumed to be spherical and have a Marshall-Palmer (exponential) distribution of sizes. The second step, described in the next chapter, is computing the distribution of radiation emerging from the atmosphere due to emission, attenuation, and multiple scattering of radiation in the medium.

2.1 Microwave Atmospheric Absorption

In the microwave portion of the spectrum the significant atmospheric gaseous absorbers are oxygen and water vapor. Oxygen attenuates through its magnetic dipole moment in a band near 60 GHz and a line at 118.75 GHz. Water vapor has rotational bands due to its electric dipole moment at 22 and 183 GHz. In addition there is continuum absorption in the windows due to water vapor, presumably from the far wing contribution of many high frequency lines. Figure 2.1 shows the total vertical attenuation as a function of frequency for the US standard atmosphere with no moisture and also fully saturated.

The absorption of microwaves by liquid cloud droplets can be combined with that due to gases. Cloud droplets (diameters less than 50 micron) are very small compared to the microwave wavelengths. In this part of the Rayleigh regime the scattering of radiation is negligible compared to the absorption. The amount of absorption is proportional to

droplet volume and so the attenuation is conveniently proportional to the liquid water content (units of g/m^3) of the cloud.

The atmospheric absorption model used in this research is a modified version of Liebe's millimeter wave propagation model (Liebe 1985). The model can compute the attenuation due to oxygen, water vapor, and cloud water from 1 to 1000 GHz for heights up to 30 km. The meteorological variables specified are height, temperature, relative humidity, and cloud liquid water content for layers in the atmosphere. The temperature and humidity are linearly interpolated between the layer interfaces, while the pressure is found by integrating the hypsometric equation. Liebe's model has 48 oxygen lines and 30 water vapor lines. The Van Vleck-Weisskopf line shape with modifications by Rosenkranz for line overlap is used. The model includes an empirically fitted continuum absorption for water vapor that is linearly proportional to frequency. A Debye model for liquid water permittivity is used to compute the cloud droplet absorption.

2.2 Microwave Scattering by Hydrometeors

To determine the effect of water and ice hydrometeors on the transfer of microwave radiation, the single scattering properties of the hydrometeors must be calculated. For this study the raindrops and ice particles are taken to be spherical. In reality raindrops are deformed oblately as they fall, and ice hydrometeors may take on a variety of shapes depending on their meteorological environment. Aircraft and satellite observations show that in most cases the polarization signature from convective precipitation is small, perhaps indicating that the spherical hydrometeor approximation is useful. The particle scattering calculations are performed using an algorithm based on the Mie theory. The radiation scattering properties of a sphere depend on the size and on a bulk material property, the complex index of refraction.

2.2.1 Complex Index of Refraction of Ice and Water

The microwave scattering properties of water and ice particles are very distinct due to the large difference in the complex refractive index between water and ice. The real part of the index determines the speed of light in the material. Through interference

Microwave Gaseous Absorption

Optical depth vs Frequency (GHz)

— Saturated

— No water vapor
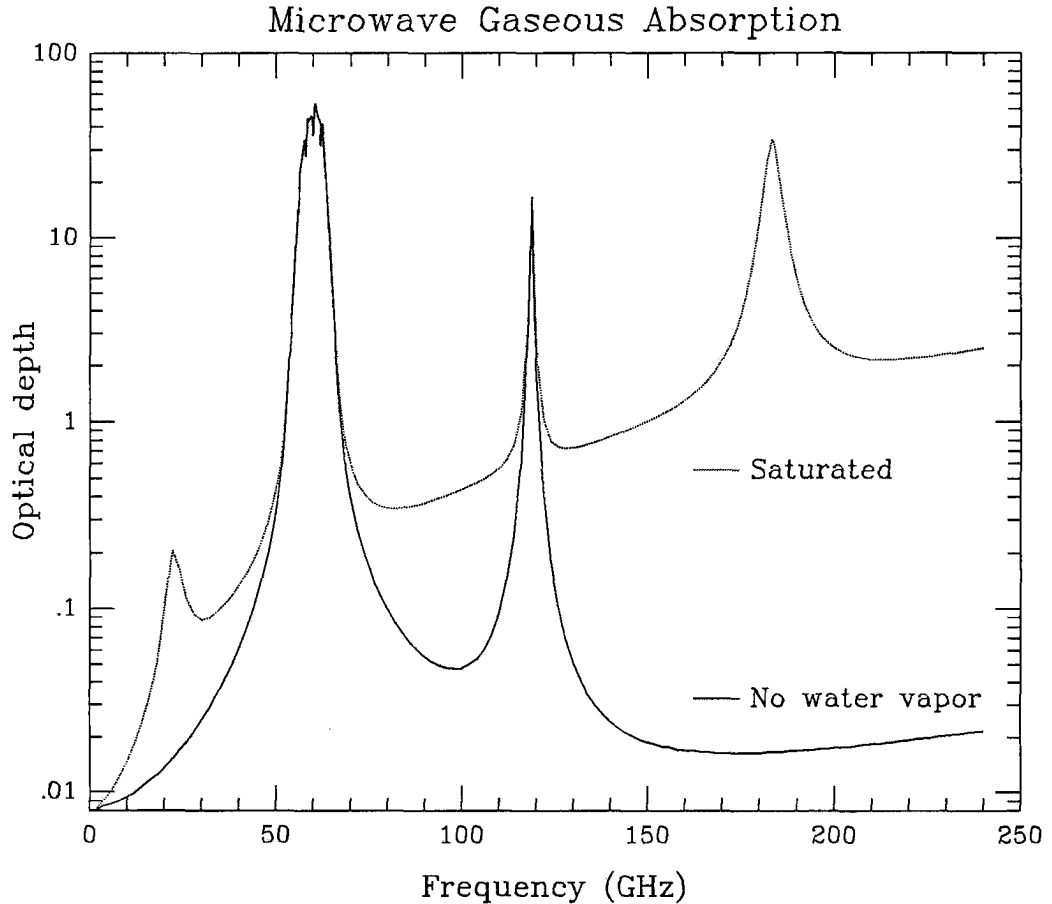
Figure 2.1: Optical depth as a function of frequency for the US standard atmosphere with no moisture and with 100% relative humidity.

effects it is the real part, along with the particle size, that governs the amount of power scattered by the particle. The imaginary part of the index determines the absorption of the material. The most important difference in the index of refraction between ice and water at microwave frequencies is that water has a large imaginary part while that of ice is very small. Over the microwave frequencies relevant for remote sensing of the atmosphere (3 GHz to 300 GHz) the real part of the index for ice is virtually constant at 1.78 and the small imaginary part increases with increasing frequency. The real part of the index for water decreases with increasing frequency from about 9 at 3 GHz to 2.5 at 300 GHz, while the imaginary part peaks near 30 GHz at around 3. The index of refraction for ice and especially for water vary significantly with temperature.

The values for the index of refraction used in this research are derived from papers by Ray (1972) for water and Warren (1984) for ice. The model for water is a modified Debye equation with temperature dependent parameters. The index values for ice were linearly interpolated in wavelength and temperature from the table in Warren. Table 2.1 shows the index of refraction for water and ice for certain pertinent remote sensing frequencies.

Table 2.1: Complex index of refraction of water and ice

Frequency (GHz)	Water (15 C)	Ice (-15 C)
6.0	(8.556,-1.601)	(1.785,-.0005)
10.7	(7.762,-2.368)	(1.785,-.0009)
19.35	(6.393,-2.869)	(1.784,-.0013)
37.0	(4.776,-2.711)	(1.784,-.0019)
85.5	(3.325,-1.893)	(1.783,-.0034)
157.0	(2.755,-1.271)	(1.782,-.0050)

2.2.2 Mie Theory

The Mie scattering theory provides a method of calculating the extinction and scattering cross-sections and the phase matrix for an ensemble of spherical particles. For a given radius r and index of refraction m the complex Mie coefficients (a_n and b_n) may be calculated (see van de Hulst, 1957 or Bohren and Huffman, 1983). These are the coefficients of the vector spherical harmonic expansion of the outgoing scattered wave, and are determined from boundary condition matching of the electro-magnetic fields. In terms of the Mie coefficients the extinction and scattering cross-sections (with units of area) are

$$
\begin{aligned}
C_{\text{ext}} &= \frac{\lambda^2}{2\pi} \sum_{n=1}^{N_t} (2n+1)\text{Re}(a_n + b_n) \\
C_{\text{sca}} &= \frac{\lambda^2}{2\pi} \sum_{n=1}^{N_t} (2n+1) \left[|a_n|^2 + |b_n|^2 \right] \ ,
\end{aligned}
\tag{2.1}
$$

where λ is the free-space wavelength. N_t is the number of terms in the Mie series that are required for high accuracy. Wiscombe (1980) showed that the number of terms needed depends on the size of the sphere, namely

$$
N_t \approx x + 4x^{1/3} + 2 \ ,
\tag{2.2}
$$

where $x = \frac{2\pi r}{\lambda}$ is the size parameter. The angular scattering amplitude functions depend on the Mie coefficients and on angular basis functions related to Legendre functions (the π_n and τ_n functions):

$$
\begin{aligned}
S_1(\cos\Theta) &= \sum_{n=1}^{N_t} \frac{2n+1}{n(n+1)} \left[a_n \pi_n(\cos\Theta) + b_n \tau_n(\cos\Theta) \right] \\
S_2(\cos\Theta) &= \sum_{n=1}^{N_t} \frac{2n+1}{n(n+1)} \left[b_n \pi_n(\cos\Theta) + a_n \tau_n(\cos\Theta) \right] ,
\end{aligned}
\tag{2.3}
$$

where Θ is the scattering angle. The four unique elements of the Stokes phase matrix are determined from the scattering amplitude functions

$$
\begin{aligned}
S_{11} &= \tfrac{1}{2} \left(|S_2|^2 + |S_1|^2 \right) & S_{12} &= \frac{1}{2} \left(|S_2|^2 - |S_1|^2 \right) \\
S_{33} &= \mathrm{Re}\left[S_2 S_1^* \right] & S_{34} &= \mathrm{Im}\left[S_2 S_1^* \right] .
\end{aligned}
\tag{2.4}
$$

The Mie theory equations described so far only pertain to a single particle. To calculate the scattering for an ensemble of particles, an integration over a size distribution is be performed. The size distribution is specified in terms of the number concentration of particles $n(r)dr$ (units of inverse volume). The extinction and scattering coefficients (units of inverse distance) are calculated by integrating the cross-sections

$$
\begin{aligned}
K_{\text{ext}} &= \int_0^\infty C_{\text{ext}}\, n(r)dr \\
K_{\text{sca}} &= \int_0^\infty C_{\text{sca}}\, n(r)dr .
\end{aligned}
\tag{2.5}
$$

The phase matrix at any scattering angle is found by integrating over size and normalizing by the scattering coefficient

$$
P_{1,2,3,4} = \frac{\lambda^2}{\pi K_{\text{sca}}} \int_0^\infty S_{11,12,33,34}\, n(r)dr
\tag{2.6}
$$

for each of the four unique elements of the scattering matrix. The integrals over the size distribution are done numerically using the trapezoidal integration formula, summing from a minimum radius to a maximum radius.

A convenient way to store the angular information in the phase matrix is to use a Legendre series representation

$$
P_i(\cos\Theta) = \sum_{l=0}^{N_l} \chi_l^{(i)} \mathcal{P}_l(\cos\Theta) .
\tag{2.7}
$$

The Legendre coefficients χ_l are found by projecting the phase matrix functions onto the Legendre polynomial basis with integration. The integration is performed numerically using Gauss-Legendre quadrature:

$$\chi_l^{(i)} = \frac{2l+1}{2} \sum_{j=1}^{N_q} w_j P_i(\mu_j) \mathcal{P}_l(\mu_j) , \qquad (2.8)$$

where the Legendre polynomials $\mathcal{P}_l(\mu)$ are obtained using upward recurrence (Abramowitz and Stegun 1972). The number of terms in the quadrature sum (N_q) is determined by the criterion that the sum should exactly represent the integral, i.e. the degree of the integrand must be less than or equal to $2N_q - 1$. The degree of the phase matrix element is $2N_t$, and the highest degree of the Legendre polynomial is N_l, so $N_l + 2N_t \leq 2N_q - 1$. To capture the angular structure of the phase matrix completely requires that $N_l = 2N_t$. To limit the computation in the radiative transfer model, however, it may be desirable to reduce the number of terms in the Legendre series (N_l). In this case the number of terms in the Mie series may as well be reduced to $N_t \leq N_l$.

The total extinction is the sum of gaseous absorption and extinction due to particles. The single scatter albedo is the particle scattering coefficient divided by the total extinction coefficient, that is

$$\kappa = K_{\text{ext}} + K_{\text{gas}}$$
$$\tilde{\omega} = \frac{K_{\text{sca}}}{\kappa} . \qquad (2.9)$$

2.2.3 Particle Size Distribution

The size distribution used in the Mie calculations was a flexible analytical function called the modified gamma distribution:

$$n(r) = ar^\alpha \exp\left(-br^\gamma\right) \qquad (2.10)$$

A size distribution that is often used for precipitation is the Marshall-Palmer distribution. This is an exponential distribution which is a special case of the gamma distribution.

$$n(r) = a \exp\left(-br\right) \qquad a = 0.16 \text{ cm}^{-4} , \quad b = 82R^{-0.21} \text{ cm}^{-1} , \qquad (2.11)$$

where R is the rain rate in mm/hr. For a given type of hydrometeor the Marshall-Palmer distribution is entirely specified by the rain rate and the maximum radius. The constants used in this distribution are most appropriate for stratiform rain. It should be remembered that, while the Marshall-Palmer distribution is very widely used, actual drop size distributions deviate significantly from the exponential form, and more importantly the parameters a and b vary widely in different types of rain.

Chapter 3

RADIATIVE TRANSFER MODEL

3.1 Rational for the Radiative Transfer Model

The radiative transfer model developed for this research is monochromatic, plane-parallel, polarized, and multi-stream. Monochromaticity works well for precipitation remote sensing applications in the microwave because scattering and absorption properties vary little over the bandwidths of instruments in use (in general, absorption line channels are not used for precipitation retrieval). The plane-parallel approximation is on less sturdy ground. It can be justified, however, by both physical arguments and practical concerns. If the microwave observations have spatial resolution comparable to the scale of precipitation (≈ 10 km) (which TRMM will have), the beam filling problem is largely alleviated. When using data from radiometers the geometry of the observation must, of course, be taken into account. But for theoretical studies where the vertical structure of precipitation is simplified, it seems reasonable to simplify the horizontal structure as well. A full three-dimensional (3D) multi-stream model is impractical. Besides the daunting complexity of such a model, computers at this time are neither fast enough nor have enough memory for such calculations. There are also problems with getting a realistic 3D precipitation structure for a 3D model.

A multi-stream model was chosen for its higher accuracy over simpler two- stream models. For microwave radiative transfer the axisymmetry and smooth phase functions allow the computer running times to be modest. Passive microwave observations have shown that polarization is mainly from wet surfaces rather than from particles (Spencer et al. 1989), presumably because precipitation sized particles are usually tumbling randomly or approximately spherical. The radiative transfer model presented here deals with

scattering from randomly oriented particles with a plane of symmetry. For high accuracy the model treats polarization completely generally because there is some coupling between the polarizations. A modification of the model allows it to study oriented non-spherical particles where the polarization effects are very strong. The model can have solar as well as thermal sources of radiation. While only thermal sources are relevant for microwave radiative transfer, the solar source is used for testing of the model.

3.2 Polarized Radiative Transfer

3.2.1 Stokes Parameters

The four Stokes parameters (I, Q, U, V) provide a complete description of the polarization state of radiation. The Stokes parameters have units of intensity (or power, the square of the electric field amplitude). This allows the Stokes parameters of multiple incoherent waves to be simply added to get the total polarization state of a radiation field. Since multiple scattering radiative transfer is a incoherent linear process, it is natural to use Stokes parameters to describe polarized radiation.

The Stokes parameters may be expressed in terms of the complex electric field vector (E_V, E_H) for a simple wave by

$$
\begin{aligned}
I &= |E_V|^2 + |E_H|^2 \\
Q &= |E_V|^2 - |E_H|^2 \\
U &= 2|E_V||E_H|\cos\delta \\
V &= 2|E_V||E_H|\sin\delta \;,
\end{aligned}
\tag{3.1}
$$

where δ is the phase difference between E_V and E_H.

An alternative set of Stokes parameters, that separates the vertical and horizontal components, is related to the set used in this research (I, Q, U, V) by

$$
I_V = I + Q \qquad I_H = I - Q \;.
\tag{3.2}
$$

A radiation field is made up of a very large number of simple waves. Since the Stokes parameters of the simple waves are added, the total polarization may range anywhere from

unpolarized ($Q = U = V = 0$) to totally polarized ($I^2 = Q^2 + U^2 + V^2$). In general, pure polarized light is elliptically polarized, for which the Stokes parameters may be expressed in terms of the ellipticity $\tan\beta$ and the direction of polarization χ:

$$
\begin{aligned}
Q &= I \cos 2\beta \cos 2\chi \\
U &= I \cos 2\beta \sin 2\chi \\
V &= I \sin 2\beta \ .
\end{aligned}
\tag{3.3}
$$

Two special cases are of interest: linear polarization has zero ellipticity and circular polarization has ellipticity of ± 1. Parameters Q and U depend on χ and therefore are dependent on the orientation of the coordinate axes.

3.2.2 Plane–Parallel Radiative Transfer Equation for Polarized Radiation

The monochromatic plane-parallel polarized radiative transfer equation for randomly oriented particles has the same form as the non-polarized equation, but with a vector of Stokes parameters replacing the scalar radiance and a scattering matrix replacing the phase function:

$$
\mu \frac{d\mathbf{I}(\tau,\mu,\phi)}{d\tau} = -\mathbf{I}(\tau,\mu,\phi) + \frac{\tilde{\omega}}{4\pi} \int_0^{2\pi} \int_{-1}^{1} \overline{\overline{M}}\,(\mu,\phi;\mu',\phi')\ \mathbf{I}(\tau,\mu',\phi')d\mu'd\phi' + \sigma(\tau,\mu,\phi)
\tag{3.4}
$$

where,
> $\mathbf{I}$ is the four vector of Stokes parameters,
> $\overline{\overline{M}}$ is the four–by–four scattering matrix,
> σ is the Stokes vector of radiation sources,
> $\tilde{\omega}$ is the single scatter albedo,
> τ is the optical depth,
> μ is the cosine of the zenith angle, and
> ϕ is the azimuth angle.

The coordinate system used here is that τ increases downward and μ is positive for downward directions.

The radiation field is separated into a collimated component (from the sun) and a diffuse component. The radiative transfer equation above involves only the diffuse component. The collimated direct solar beam is attenuated according to Beer's Law (by

$e^{-\tau/\mu}$). The collimated component is scattered by the medium and becomes a "pseudo-source" of diffuse radiation. Along with this solar source there is also the source of radiation due to thermal emission of the medium. Together, the two sources of radiation are expressed as a vector by

$$
\sigma(\mu,\phi) = (1-\tilde{\omega})B(T)\begin{pmatrix} 1 \\ 0 \\ 0 \\ 0 \end{pmatrix} + \frac{F_0}{\mu_0}\frac{\tilde{\omega}}{4\pi}\exp(-\tau/\mu_0)\,\overline{\overline{M}}\,(\mu,\phi;\mu_0,\phi_0)\cdot\begin{pmatrix} 1 \\ 0 \\ 0 \\ 0 \end{pmatrix} \quad (3.5)
$$

where $B(T)$ is the Planck blackbody function, F_0 is the direct solar flux at the top of the atmosphere, and (μ_0,ϕ_0) is the direction of the direct beam. The source terms contain the $\begin{pmatrix} 1 \\ 0 \\ 0 \\ 0 \end{pmatrix}$ vector because both thermal emission and solar radiation are unpolarized. In this formulation the reflection of the direct solar beam from a specular ground surface is not included.

The Planck blackbody function $B(T)$ in units of Watts/(meter^2 ster micron) is

$$
B(T) = \frac{1.1911 \times 10^8}{\lambda^5\left[\exp\left(\frac{1.4388\times10^4}{\lambda T}\right) - 1\right]} , \quad (3.6)
$$

where λ is the wavelength in microns and T is the temperature in Kelvins. In the microwave portion of the spectrum, where the energy of a photon is much less than the thermal energy, the Rayleigh-Jeans approximation,

$$
B(T) \approx \frac{2kc}{\lambda^4}T , \quad (3.7)
$$

may be used. Since the Planck function is proportional to temperature, radiation intensity may be expressed directly as a brightness temperature, in which case $B(T) = T$. The Rayleigh-Jeans approximation is accurate as long as $\frac{h\nu}{kT} \ll 1$ (e.g. for $\nu = 157$ GHz and $T = 250°$K the error is 1.5%). It is important to realize that brightness temperature is a separate scale of radiance, and its correspondence to (W m^{-2} sr^{-1} μm^{-1}) is only tested upon emission from a source at a physical temperature. For example, discussion of a 1.0°K brightness temperature difference is valid even though 1.0°K is out of the Rayleigh-Jeans limit for frequencies considered here.

3.2.3 The Polarization Scattering Matrix

Besides the radiance being a vector rather than a scalar, there is another complexity to polarized radiative transfer that occurs because the definition of the Q and U Stokes parameters requires a reference frame. For single scattering the reference frame is naturally the scattering plane, while for a plane–parallel radiative transfer calculation the convenient reference frame is the meridional plane (defined by the z-axis and the direction of travel). More specifically, the polarization axes for single scattering are perpendicular to the scattering plane (H) and in the scattering plane, perpendicular to the direction of travel (V); in the radiative transfer model the polarization axes are perpendicular to the meridional plane (II) and in the meridional plane, perpendicular to the direction of travel (V).

Since single scattering calculations (e.g. Mie calculations) provide the phase matrix in terms of the scattering plane, a polarization transformation is necessary before the phase matrix can be used in the radiative transfer model (see Chandrasekhar 1960 or Hovenier 1969). The polarization reference plane is rotated from the incident meridional plane to the scattering plane; the single scattering transformation represented by the phase matrix is applied; and, the polarization is rotated to the outgoing meridional plane (see figure 3.1). This transformation is expressed mathematically by

$$\overline{\overline{M}}\left(\theta, \phi; \theta', \phi'\right) = \overline{\overline{L}}\left(i_2 - \pi\right)\overline{\overline{P}}\left(\cos\Theta\right)\overline{\overline{L}}\left(i_1\right) . \qquad (3.8)$$

For the (I, Q, U, V) Stokes basis the polarization rotation matrix is

$$\overline{\overline{L}}(i) = \begin{pmatrix} 1 & 0 & 0 & 0 \\ 0 & \cos 2i & -\sin 2i & 0 \\ 0 & \sin 2i & \cos 2i & 0 \\ 0 & 0 & 0 & 1 \end{pmatrix} , \qquad (3.9)$$

where the rotation angle i_1 is the angle between the incoming ray (θ', ϕ') and the scattering plane, and i_2 is the angle between the outgoing ray (θ, ϕ) and the scattering plane.
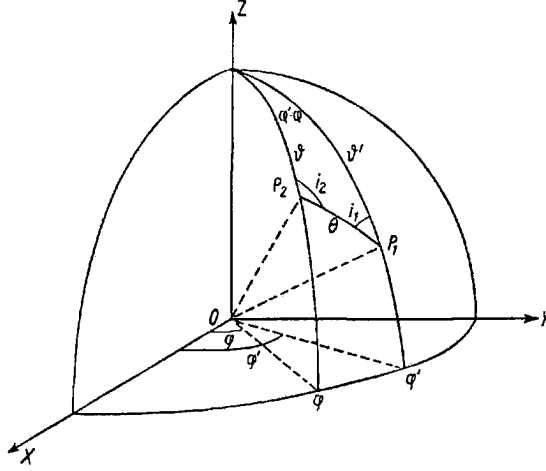
Figure 3.1: Illustration of the rotation of the polarization reference frame. The polarization of the incident ray (θ', ϕ') is in terms of the P_1OZ plane, and of the outgoing ray (θ, ϕ) in terms of the P_2OZ plane. The polarization is rotated into the scattering plane (P_1OP_2) by angle i_1, the phase matrix is applied, and then the polarization is rotated out of the plane by i_2.

The scattering angle Θ and the polarization rotation angles i_1 and i_2 may be found from spherical trigonometry by

$$\cos \Theta = \cos \theta' \cos \theta + \sin \theta' \sin \theta \cos(\phi' - \phi) \tag{3.10}$$

$$\sin i_1 = \sin \theta \sin(\phi' - \phi)/\sin \Theta \tag{3.11}$$

$$\sin i_2 = \sin \theta' \sin(\phi' - \phi)/\sin \Theta \tag{3.12}$$

$$\cos i_1 = \left(\sin \theta' \cos \theta - \sin \theta \cos \theta' \cos(\phi' - \phi)\right)/\sin \Theta \tag{3.13}$$

$$\cos i_2 = \left(\sin \theta \cos \theta' - \sin \theta' \cos \theta \cos(\phi' - \phi)\right)/\sin \Theta . \tag{3.14}$$

For randomly oriented particles with a plane of symmetry the sixteen element phase matrix has only six unique values (Hovenier 1969):

$$\overline{\overline{P}}(\cos \Theta) = \begin{pmatrix} P_1 & P_2 & 0 & 0 \\ P_2 & P_5 & 0 & 0 \\ 0 & 0 & P_3 & P_4 \\ 0 & 0 & -P_4 & P_6 \end{pmatrix} . \tag{3.15}$$

The phase matrix for spheres has $P_5 = P_1$ and $P_6 = P_3$.

After the polarization rotations have been done the scattering matrix has the form

$$
\overline{\overline{M}} =
\begin{pmatrix}
P_1 & P_2\cos 2i_1 & -P_2\sin 2i_1 & 0 \\[4pt]
P_2\cos 2i_2 & \begin{array}{l}P_5\cos 2i_1\cos 2i_2\\ -P_3\sin 2i_1\sin 2i_2\end{array} & \begin{array}{l}-P_5\sin 2i_1\cos 2i_2\\ -P_3\cos 2i_1\sin 2i_2\end{array} & -P_4\sin 2i_2 \\[10pt]
P_2\sin 2i_2 & \begin{array}{l}P_5\cos 2i_1\sin 2i_2\\ +P_3\sin 2i_1\cos 2i_2\end{array} & \begin{array}{l}-P_5\sin 2i_1\sin 2i_2\\ +P_3\cos 2i_1\cos 2i_2\end{array} & P_4\cos 2i_2 \\[10pt]
0 & -P_4\sin 2i_1 & -P_4\cos 2i_1 & P_6
\end{pmatrix}
\tag{3.16}
$$

3.3 Derivation of the Matrix Form of the Radiative Transfer Equation

3.3.1 Fourier Transforming in Azimuth

The azimuthal angle is discretized by expressing the azimuthal dependence in a Fourier series. A real function of azimuth $F(\phi)$ is expanded in a finite series

$$
F(\phi) = \sum_{m=0}^{M} F_m^c \cos\phi + F_m^s \sin\phi \qquad F_0^s = 0 \tag{3.17}
$$

with the sines and cosines forming an orthogonal set of functions

$$
\begin{array}{l}
\int_0^{2\pi} \cos m\phi \cos m'\phi = c_m^c \delta_{mm'} \\[6pt]
\int_0^{2\pi} \sin m\phi \sin m'\phi = c_m^s \delta_{mm'} \\[6pt]
\int_0^{2\pi} \cos m\phi \sin m'\phi = 0
\end{array}
\qquad
c_m^r =
\begin{cases}
2\pi & r=c,\; m=0 \\
0 & r=s,\; m=0 \\
\pi & m>0
\end{cases}
. \tag{3.18}
$$

The integral over azimuth of a product of functions transforms to a sum of the product of the Fourier coefficients

$$
\int_0^{2\pi} A(\phi)B(\phi)d\phi = \sum_{m=0}^{M}\sum_{r=c,s} c_m^r A_m^r B_m^r \tag{3.19}
$$

The radiative transfer equation then transforms to

$$
\mu\frac{d\mathbf{I}_{mr}}{d\tau} = -\mathbf{I}_{mr} + \frac{\tilde{\omega}}{4\pi}\sum_{m'=0}^{M}\sum_{r'=c,s} c_{m'}^{r'}\int_{-1}^{1}\overline{\overline{M}}_{mm'rr'}(\mu,\mu')\mathbf{I}_{m'r'}(\mu')d\mu' + \sigma_{mr}(\mu) \tag{3.20}
$$

$$
m = 0,1,\ldots,M \;, \qquad r = c,s
$$

where the m subscript refers to the azimuthal Fourier mode, and the r subscript refers to the cosine and sine terms. The Fourier expansion is done separately for each element of the Stokes radiance vectors and the scattering matrix.

3.3.2 Discretization in Zenith Angle

The zenith angle variable, μ, is divided up into a number of discrete angles chosen by a numerical quadrature scheme. A quadrature formula provides a set of abscissae (μ_i) and weights (w_i) that are used to approximate an integral accurately, by

$$\int_{-1}^{1} F(\mu)d\mu \approx \sum_{j=1}^{N} w_j \left[F(-\mu_j) + F(+\mu_j) \right] . \tag{3.21}$$

There are N angles in each hemisphere of solid angle (upward and downward). The radiative transfer code has the choice of five quadrature schemes: Gaussian, double Gaussian, Lobatto, and two schemes where the user can choose the angles (see appendix A). For low enough powers in μ the quadrature sum equals the integral exactly.

Replacing the integral over μ in the radiative transfer equation by the quadrature sum gives

$$\pm\mu_j \frac{d\mathbf{I}_{mr}(\tau, \pm\mu_j)}{d\tau} = -\mathbf{I}_{mr}(\tau, \pm\mu_j) + \sigma_{mr}(\tau, \pm\mu_j)$$

$$+ \frac{\tilde{\omega}}{4\pi} \sum_{m'=0}^{M} \sum_{r'=c,s} \sum_{j'=1}^{N} c_{m'}^{r'} w_{j'} \left[\overline{\overline{M}}_{mm'rr'}(\pm\mu_j, +\mu_{j'}) \, \mathbf{I}_{m'r'}(\tau, +\mu_{j'}) \right.$$

$$\left. + \overline{\overline{M}}_{mm'rr'}(\pm\mu_j, -\mu_{j'}) \, \mathbf{I}_{m'r'}(\tau, -\mu_{j'}) \right] \tag{3.22}$$

$$j = 1, \ldots, N \qquad m = 0, \ldots, M \qquad r = c, s$$

There are two quadrature sums; one for each hemisphere of the scattering integral.

3.3.3 Calculation of the Radiative Transfer Scattering Matrix

As described in section 2.2 the single scattering phase matrix $\overline{\overline{P}}$ is conveniently expressed as a Legendre series

$$\overline{\overline{P}}(\cos\Theta) = \sum_{l=0}^{N_l} \overline{\overline{\chi}}_l \mathcal{P}_l(\cos\Theta) , \tag{3.23}$$

where $\mathcal{P}_l$ is the l'th order Legendre polynomial and $\overline{\overline{\chi}}_l$ is the l'th Legendre coefficient matrix. In the scalar (unpolarized) radiative transfer case the Fourier modes of the phase function $p_m(\mu, \mu')$ are calculated from the coefficients of the Legendre series using the addition theorem of associated Legendre functions. The rotation of the reference frame of the polarization precludes that method of finding the Fourier modes of the scattering

matrix. Dave (1970) invented a very complicated series method to calculate the modes of the scattering matrix. A new simpler method was used for this model. The method used here is to perform the polarization rotation explicitly in azimuth space and then Fourier transform the results to get the scattering matrix for each Fourier azimuth mode. This method is similar to that of Ishimaru et al. (1984), except the rotation is performed on the Stokes parameters rather than the scattering amplitudes.

For each pair of quadrature angles μ_j and $\mu_{j'}$ (outgoing and incoming directions) and for a number of azimuth angles $\Delta\phi_k = \phi' - \phi$, the scattering angle Θ is found, and the Legendre series is summed for the six unique elements of the phase matrix. Equation (3.16) is used to to obtain the scattering matrix $\overline{\overline{M}}$ having the desired polarization reference frame. The azimuth angle differences are at equally spaced angles

$$\Delta\phi_k = \frac{2\pi k}{N_\phi} \quad k = 0, 1, \ldots, N_\phi - 1 , \tag{3.24}$$

where N_ϕ is chosen so that the highest frequency in $\Delta\phi$ is completely sampled, that is

$$N_\phi = 2^{[\log_2(N_l+4)+1]+1} . \tag{3.25}$$

The scattering matrix $\overline{\overline{M}}$ is then Fourier transformed to obtain the Fourier series representation

$$\overline{\overline{M}}(\mu_j, \mu_{j'}, \phi' - \phi) = \sum_{m=0}^{M} \left[\overline{\overline{M}}_m^c(\mu_j, \mu_{j'}) \cos m(\phi' - \phi) + \overline{\overline{M}}_m^s(\mu_j, \mu_{j'}) \sin m(\phi' - \phi) \right] . \tag{3.26}$$

This form of the scattering matrix $\overline{\overline{M}}$ is not quite what is needed because it has one Fourier series in $\phi' - \phi$ rather than a Fourier series separately for ϕ' and ϕ, such as

$$
\begin{aligned}
\overline{\overline{M}}(\mu_j, \mu_{j'}, \phi, \phi') &= \sum_{m=0}^{M} \sum_{m'=0}^{M} \left[\overline{\overline{M}}_{mm'}^{cc} \cos m\phi \cos m'\phi' + \overline{\overline{M}}_{mm'}^{cs} \cos m\phi \sin m'\phi' \right. \\
&\quad \left. + \overline{\overline{M}}_{mm'}^{sc} \sin m\phi \cos m'\phi' + \overline{\overline{M}}_{mm'}^{ss} \sin m\phi \sin m'\phi' \right] .
\end{aligned} \tag{3.27}
$$

Using the angle addition formulae for cosine and sine it is easy to show that the coefficients for the double Fourier series are simply related to the single Fourier series coefficients by

$$
\begin{aligned}
\overline{\overline{M}}_{mm'}^{cc} &= \overline{\overline{M}}_{mm'}^{ss} = \overline{\overline{M}}_m^c \delta_{mm'} \\
\overline{\overline{M}}_{mm'}^{cs} &= -\overline{\overline{M}}_{mm'}^{sc} = \overline{\overline{M}}_m^s \delta_{mm'} .
\end{aligned} \tag{3.28}
$$

Since the scattering matrix only depends on the difference in azimuth between the incoming and outgoing angles, the azimuth Fourier modes separate ($\overline{\overline{M}}$ depends only on m, rather than m and m'). This property allows the azimuth modes to be solved separately, thus reducing the computational burden. In the scalar radiative transfer case the scattering function depends only on $\cos m(\phi' - \phi)$, so the $\overline{\overline{M}}_{mm'}^{cs}$ and $\overline{\overline{M}}_{mm'}^{sc}$ terms are zero, and cosine and sine terms don't mix.

The explicit form of the scattering matrix given in equation (3.16) shows some of its special symmetries. The upper left and lower right two by two blocks are even functions in $\Delta\phi$, while the upper right and lower left blocks are odd functions. This means the cosine matrices have off-diagonal blocks of zeros, and the sine matrices have diagonal blocks of zeros. Another way of stating this symmetry is that negating ϕ and ϕ' results in negating the off-diagonal blocks. This allows trivial calculation of the scattering matrix for $\pi < \Delta\phi \leq 2\pi$ from the values for $0 < \Delta\phi \leq \pi$. Another related symmetry is that negating μ and μ' results again in negating the off-diagonal blocks. This is due to the invariance of the scattering matrix under rotation of the coordinate system ($\mu \rightarrow -\mu$ and $\phi \rightarrow -\phi$): $\overline{\overline{M}}(\mu, \mu', \phi' - \phi) = \overline{\overline{M}}(-\mu, -\mu', \phi - \phi')$.

For a given azimuth mode m the cosine and sine scattering matrices can be combined into a single eight-by-eight scattering matrix showing the blocks that are repeated and those that are zero:

$$
\begin{pmatrix} I^c \\ Q^c \\ U^c \\ V^c \\ I^s \\ Q^s \\ U^s \\ V^s \end{pmatrix}_{out} = \left(\begin{array}{cc|cc|cc|cc} M_{11}^c & M_{12}^c & 0 & 0 & 0 & 0 & M_{13}^s & M_{14}^s \\ M_{21}^c & M_{22}^c & 0 & 0 & 0 & 0 & M_{23}^s & M_{24}^s \\ 0 & 0 & M_{33}^c & M_{34}^c & M_{31}^s & M_{32}^s & 0 & 0 \\ 0 & 0 & M_{43}^c & M_{44}^c & M_{41}^s & M_{42}^s & 0 & 0 \\ 0 & 0 & -M_{13}^s & -M_{14}^s & M_{11}^c & M_{12}^c & 0 & 0 \\ 0 & 0 & -M_{23}^s & -M_{24}^s & M_{21}^c & M_{22}^c & 0 & 0 \\ -M_{31}^s & -M_{32}^s & 0 & 0 & 0 & 0 & M_{33}^c & M_{34}^c \\ -M_{41}^s & -M_{42}^s & 0 & 0 & 0 & 0 & M_{43}^c & M_{44}^c \end{array} \right) \begin{pmatrix} I^c \\ Q^c \\ U^c \\ V^c \\ I^s \\ Q^s \\ U^s \\ V^s \end{pmatrix}_{in}
$$

(3.29)

where c refers to the cosine Fourier azimuth mode and s to the sine mode.

The blocks of zeros in this scattering matrix suggest a computationally efficient rearrangement of the cosine and sine modes of the Stokes parameters. If the Stokes radiance

vectors are written as

$$\hat{\mathbf{I}}^c = \begin{pmatrix} I^c \\ Q^c \\ U^s \\ V^s \end{pmatrix} \qquad \hat{\mathbf{I}}^s = \begin{pmatrix} I^s \\ Q^s \\ U^c \\ V^c \end{pmatrix} , \tag{3.30}$$

then the $\hat{\mathbf{I}}^c$ and $\hat{\mathbf{I}}^s$ radiance vectors decouple. The rows and columns of the scattering matrix rearrange to give two separate four-by-four matrices

$$\hat{\mathbf{I}}_{\text{out}}^c = \begin{pmatrix} M_{11}^c & M_{12}^c & M_{13}^s & M_{14}^s \\ M_{21}^c & M_{22}^c & M_{23}^s & M_{24}^s \\ -M_{31}^s & -M_{32}^s & M_{33}^c & M_{34}^c \\ -M_{41}^s & -M_{42}^s & M_{43}^c & M_{44}^c \end{pmatrix} \hat{\mathbf{I}}_{\text{in}}^c \tag{3.31}$$

$$\hat{\mathbf{I}}_{\text{out}}^s = \begin{pmatrix} M_{11}^c & M_{12}^c & -M_{13}^s & -M_{14}^s \\ M_{21}^c & M_{22}^c & -M_{23}^s & -M_{24}^s \\ M_{31}^s & M_{32}^s & M_{33}^c & M_{34}^c \\ M_{41}^s & M_{42}^s & M_{43}^c & M_{44}^c \end{pmatrix} \hat{\mathbf{I}}_{\text{in}}^s . \tag{3.32}$$

Conventionally the solar azimuth is set to zero, so both the solar and thermal sources of radiation are even functions and unpolarized (I^c is the only non-zero element). Since the $\hat{\mathbf{I}}^c$ and $\hat{\mathbf{I}}^s$ radiance vectors are decoupled, further scattering leaves the sine mode radiance vector zero. Therefore only the first four-by-four Fourier scattering matrix need be considered. For the azimuthally symmetric case ($m = 0$) the sine terms in the scattering matrix are zero and the U and V Stokes parameters are zero, so a two-by-two scattering matrix may be used.

If the solar azimuth is zero the direction of the incident solar radiation is actually $\mu_0 = \cos\theta_0$, $\phi_0 = \pi$. In terms of the rearranged Stokes vector the solar "pseudo-source" is then

$$\hat{\sigma}_m(\mu_j) = \frac{F_0}{\mu_0} \frac{\tilde{\omega}}{4\pi} \exp(-\tau/\mu_0) \begin{pmatrix} M_{11}^c \\ M_{21}^c \\ M_{31}^s \\ M_{41}^s \end{pmatrix} , \tag{3.33}$$

where the scattering matrix elements are evaluated as described above for the quadrature angles μ_j and the solar angle μ_0.

3.3.4 Matrix Formulation of the Polarized Radiative Transfer Equation

Using the notation $\hat{\mathbf{I}}_{mj}^{\pm} = \hat{\mathbf{I}}_m^c(\tau, \pm\mu_j)$ the discretized radiative transfer equation becomes

$$\pm \mu_j \frac{d\hat{\mathbf{I}}_{mj}^{\pm}}{d\tau} = -\hat{\mathbf{I}}_{mj}^{\pm} + \hat{\sigma}_{mj}^{\pm} + \frac{\tilde{\omega}}{4\pi} \sum_{j=1}^{N} c_m w_{j'} \left[\overline{\overline{M}}_{mjj'}^{\pm+} \hat{\mathbf{I}}_{mj'}^{+} + \overline{\overline{M}}_{mjj'}^{\pm-} \hat{\mathbf{I}}_{mj'}^{-} \right] , \qquad (3.34)$$

where the plus and minus superscripts refer to the quadrature angles in the downward (+) and upward (−) directions, respectively.

The notation can be simplified by removing the decoration of subscripts and writing the transfer equation using matrices and vectors. First the dependence on τ and m is taken to be understood (the radiative transfer equation will be numerically solved separately for each Fourier azimuth mode m). The Stokes radiance vectors for each quadrature angle in a hemisphere are combined into one long radiance vector. The structure of the radiance vectors is

$$\bar{I} = \begin{pmatrix} \hat{\mathbf{I}}_{j=1} \\ \hat{\mathbf{I}}_{j=2} \\ \cdot \\ \cdot \\ \cdot \\ \hat{\mathbf{I}}_{j=N} \end{pmatrix} , \qquad \hat{\mathbf{I}}_j = \begin{pmatrix} I_j^c \\ Q_j^c \\ U_j^s \\ V_j^s \end{pmatrix} \qquad (3.35)$$

The length of the radiance vector is thus $4 \times N$. The individual scattering matrices for each pair of angles $\mu_j, \mu_{j'}$ are combined to form a scattering matrix that operates on a radiance vector to produce another vector (the discrete equivalent of integration over all angles). In matrix notation the plane–parallel polarized radiative transfer equation becomes

$$\pm \overline{\overline{D}} \frac{d\bar{I}^{\pm}}{d\tau} = -\bar{I}^{\pm} + \overline{\overline{C}}^{\pm+} \bar{I}^{+} + \overline{\overline{C}}^{\pm-} \bar{I}^{-} + \bar{\sigma}^{\pm} . \qquad (3.36)$$

The elements of the matrices $\overline{\overline{D}}$ and $\overline{\overline{C}}^{\pm\pm}$ are

$$|\overline{\overline{D}}|_{jj'ii'} = \mu_j$$

$$|\overline{\overline{C}}^{\pm\pm}|_{jj'ii'} = \frac{\tilde{\omega}}{4\pi} c_m w_{j'} |\overline{\overline{M}}_{mrjj'}^{\pm\pm}|_{ii'}$$

where the i and i' indices refer to the Stokes parameters.

3.4 Integrating the Radiative Transfer Equation

3.4.1 Finite Differencing of the Radiative Transfer Equation

The transfer equation (3.36) is a matrix first–order ordinary differential equation. One method of numerically integrating the differential equation is to approximate the derivative $(\frac{dI}{d\tau})$ by a finite difference scheme. The simplest difference scheme is

$$\frac{dI}{d\tau} = \frac{I(\tau) - I(\tau + \Delta\tau)}{\Delta\tau} \ . \tag{3.37}$$

Although simple, this method of differencing, with little added computational burden, can be as accurate as desired by choosing $\Delta\tau$ small enough.

Defining $I_0 = \bar{I}(\tau)$ and $I_1 = \bar{I}(\tau + \Delta\tau)$ equation (3.36) becomes

$$
\begin{aligned}
I_1^+ - I_0^+ &= \Delta\tau D^{-1} \left[-I_0^+ + C^{++} I_0^+ + C^{+-} I_1^- + \sigma^+ \right] \\
I_1^- - I_0^- &= \Delta\tau D^{-1} \left[-I_1^- + C^{-+} I_0^+ + C^{--} I_1^- + \sigma^- \right] \ .
\end{aligned}
\tag{3.38}
$$

A finite differencing scheme requires that the right hand side of the equation be defined in terms of the discretized values I_0 and I_1, which, of course, are nearly the same since $\Delta\tau$ is assumed very small. The particular combination of I_0 and I_1 used on the right hand side is chosen for convenience in the next section. The last equation can be rearranged to express the radiation emerging from the thin layer in terms of the incident radiation

$$
\begin{aligned}
I_1^+ &= \left[\bar{\bar{1}} - \Delta\tau D^{-1}(\bar{\bar{1}} - C^{++}) \right] I_0^+ + \Delta\tau D^{-1} C^{+-} I_1^- + \Delta\tau D^{-1}\sigma^+ \\
I_0^- &= \left[\bar{\bar{1}} - \Delta\tau D^{-1}(\bar{\bar{1}} - C^{--}) \right] I_1^- + \Delta\tau D^{-1} C^{-+} I_0^+ + \Delta\tau D^{-1}\sigma^- \ .
\end{aligned}
\tag{3.39}
$$

3.4.2 The Interaction Principle

The interaction principle is an intuitively simple way of expressing the linear interaction of radiation with a medium. The radiation emerging from any medium can be expressed in terms of the radiation incident plus the radiation generated within the medium (see figure 3.2). In the matrix formulation used here the interaction principle is

$$
\begin{aligned}
I_1^+ &= T^+ I_0^+ + R^+ I_1^- + S^+ \\
I_0^- &= T^- I_1^- + R^- I_0^+ + S^- \ ,
\end{aligned}
\tag{3.40}
$$

$$\downarrow I_0^+ \qquad\qquad \uparrow I_0^-$$

$$R^\pm \quad T^\pm \quad S^\pm$$

$$\uparrow I_1^- \qquad\qquad \downarrow I_1^+$$

Figure 3.2: A schematic illustration of the interaction principle. The I_0^+ and I_1^- on the left represent the incident radiation, and the I_0^- and I_1^+ on the right represent the emergent radiation. The R, T, and S are the reflection, transmission, and source terms, respectively, which describe how the medium interacts with the radiation.

where T is called the transmission matrix, R is called the reflection matrix, and S is called the source vector. The finite difference form of the radiative transfer equation (3.39) is the same as the interaction principle. By making the obvious associations the reflection and transmission matrices and the source vectors for the infinitesimal layer can be related to the local properties of the medium by

$$T^\pm = \left[\bar{\bar{1}} - \Delta\tau D^{-1}(\bar{\bar{1}} - C^{\pm\pm})\right]$$

$$R^\pm = \Delta\tau D^{-1} C^{\pm\mp}$$

$$S^\pm = \Delta\tau D^{-1} \sigma^\pm . \tag{3.41}$$

Relating of the radiative transfer equation to the interaction principle is usually called initialization. There are a number of different initialization methods (see Wiscombe 1976b), each corresponding to a particular type of finite difference scheme. The method used here is sometimes called infinitesimal generator initialization.

3.4.3 The Adding Algorithm

The previous sections have shown how the coefficients in the radiative transfer equation relate to the reflection and transmission matrices and source vectors for infinitesimal layers. What is needed now is an integration procedure to relate the properties of infinitesimal layers to the properties of an atmosphere containing many finite layers. With the reflection and transmission matrices and source vectors for the whole medium, the interaction principle can be applied to the incident radiation at the boundaries to calculate the outgoing radiation. The radiation field inside the medium may also be calculated

from the incident radiation and the matrices for the medium above and below the level of interest.

The interaction principle is used to derive a formula for combining (adding) two layers, i.e. to express the reflection and transmission matrices and source vectors for the combined layer in terms of the individual layer matrices and vectors. Starting with the interaction principles for two adjacent layers (see figure 3.3), the radiance at the interface (I_1^+, I_1^-) may be eliminated and the equations rearranged into the form of the interaction principle for the combined layer. The resulting reflection and transmission matrices and source vectors are

$$R_T^+ = R_2^+ + T_2^+ \Gamma^+ R_1^+ T_2^- \; , \qquad R_T^- = R_1^- + T_1^- \Gamma^- R_2^- T_1^+$$

$$T_T^+ = T_2^+ \Gamma^+ T_1^+ \; , \qquad T_T^- = T_1^- \Gamma^- T_2^-$$

$$S_T^+ = S_2^+ + T_2^+ \Gamma^+ (S_1^+ + R_1^+ S_2^-) \; , \qquad S_T^- = S_1^- + T_1^- \Gamma^- (S_2^- + R_2^- S_1^+)$$

$$\Gamma^+ = \left[1 - R_1^+ R_2^- \right]^{-1} \; , \qquad \Gamma^- = \left[1 - R_2^- R_1^+ \right]^{-1} \; . \qquad (3.42)$$

The adding formulae may be physically interpreted in terms of multiply reflected rays, with the Γ factors being the multiple reflection factors.

By a similar manipulation of the interaction principles for two layers, the internal radiance (I_1^+, I_1^-) may be expressed in terms of the radiance incident upon the two layers

$$I_1^+ = \Gamma^+ \left[R_1^+ T_2^- I_2^- + T_1^+ I_0^+ + R_1^+ S_2^- + S_1^+ \right]$$

$$I_1^- = \Gamma^- \left[R_2^- T_1^+ I_0^+ + T_2^- I_2^- + R_2^- S_1^+ + S_2^- \right] \; . \qquad (3.43)$$

3.4.4 The Doubling Algorithm

The radiative properties for a finite layer could be calculated by using the adding algorithm to combine very many thin layers (millions of thin layers could be required, depending on the final optical depth and the desired accuracy). Fortunately there is a much faster method of building up a thick layer from many identical thin layers: the doubling algorithm. Doubling is really just the adding algorithm applied in a special way. Imagine many identical thin layers of optical depth $\Delta \tau$. Combining two layers with the

$$\downarrow I_0^+ \qquad\qquad \uparrow I_0^-$$

$R_1^{\pm}$	$T_1^{\pm}$	$S_1^{\pm}$	$\uparrow I_1^-$
$R_2^{\pm}$	$T_2^{\pm}$	$S_2^{\pm}$	$\downarrow I_1^+$

$$\uparrow I_2^- \qquad\qquad \downarrow I_2^+$$

Figure 3.3: A schematic illustration of adding two layers. The reflection (R), transmission (T), and source (S) terms which describe each layer (1 and 2) are combined to make the R, T, and S terms for the combined layer.

adding method gives a layer with an optical depth of $2\Delta\tau$. Since all of the thin layers are the same, all $2\Delta\tau$ thick layers will be the same, and the doubled layer can be added to itself to produce a $4\Delta\tau$ thick layer. After N of these doubling steps the layer is built up to an optical depth of $2^N \Delta\tau$ (a million thin layers takes 20 steps). The doubling formulae for the reflection and transmission matrices are

$$R_{2N}^+ = R_N^+ + T_N^+ \Gamma^+ R_N^+ T_N^- \quad , \quad R_{2N}^- = R_N^- + T_N^- \Gamma^- R_N^- T_N^+$$

$$T_{2N}^+ = T_N^+ \Gamma^+ T_N^+ \quad , \quad T_{2N}^- = T_N^- \Gamma^- T_N^-$$

$$\Gamma^+ = \left[1 - R_N^+ R_N^-\right]^{-1} \quad , \quad \Gamma^- = \left[1 - R_N^- R_N^+\right]^{-1} . \tag{3.44}$$

The doubling, adding, and finite generator initialization algorithms presented here were developed by Grant and Hunt (1969). The doubling method described so far requires that the finite layer be uniform. The solar pseudo-source, however, has an exponential dependence with optical depth, and it also is desirable to have the thermal emission vary with depth. The doubling method has been extended by Wiscombe (1976a) to incorporate sources that vary exponentially with optical depth and sources that vary linearly with optical depth. With exponential sources the source at a deeper optical depth is the same as the source at a lower optical depth except for a multiplicative factor. This introduces a factor into the formulae for adding the sources of two layers

$$S_{2N}^+ = \gamma^N S_N^+ + T_N^+ \Gamma^+ \left(S_N^+ + R_N^+ S_N^- \gamma^N\right)$$

$$S_{2N}^- = S_N^- + T_N^- \Gamma^- \left(S_N^- \gamma^N + R_N^- S_N^+\right)$$

$$\gamma = \exp(-\Delta\tau/\mu_0) . \tag{3.45}$$

For linear sources, the source at a deeper optical depth is the same as the source at a lower optical depth except for an additive factor. This introduces an extra complication of requiring a doubling sequence for a separate vector $C^\pm$, which is what the source vector would be if the source did not vary with optical depth:

$$
\begin{aligned}
S_{2N}^+ &= (S_N^+ + N\alpha C_N^+) + T_N^+ \Gamma^+ \left[S_N^+ + R_N^+ (S_N^- + N\alpha C_N^-) \right] \\
S_{2N}^- &= S_N^- + T_N^- \Gamma^- \left[(S_N^- + N\alpha C_N^-) + R_N^- S_N^+ \right] \\
C_{2N}^+ &= C_N^+ + T_N^+ \Gamma^+ \left[C_N^+ + R_N^+ C_N^- \right] \\
C_{2N}^- &= C_N^- + T_N^- \Gamma^- \left[C_N^- + R_N^- C_N^+ \right] \\
\alpha &= \left[\frac{B(\tau_1)}{B(\tau_0)} - 1 \right] \frac{\Delta \tau}{(\tau_1 - \tau_0)} .
\end{aligned}
\tag{3.46}
$$

3.4.5 Purely Absorbing Layers

For layers that have no scattering the reflection and transmission matrices and source vectors can be calculated directly without resorting to the doubling algorithm. For a non-scattering layer there is no reflection, and the transmission is simply the transmission for the given optical depth. The radiation emitted by the layer is unpolarized and azimuthally symmetric. For a source that is linear in optical depth the following formulae apply

$$
\begin{aligned}
|R^\pm|_{jj'ii'} &= 0 , \\
|T^\pm|_{jj'ii'} &= \exp(-\Delta\tau/\mu_j)\delta_{jj'}\delta_{ii'} , \\
|S^+|_{ji} &= \left\{ B_0 + \frac{\Delta B}{\Delta \tau} - \left[B_0 + \frac{\Delta B}{\Delta \tau}\mu_j \left(1 + \frac{\Delta\tau}{\mu_j} \right) \right] \exp(-\Delta\tau/\mu_j) \right\} \delta_{m,0}\delta_{i,1} , \\
|S^-|_{ji} &= \left\{ B_1 - \frac{\Delta B}{\Delta \tau} - \left[B_1 - \frac{\Delta B}{\Delta \tau}\mu_j \left(1 + \frac{\Delta\tau}{\mu_j} \right) \right] \exp(-\Delta\tau/\mu_j) \right\} \delta_{m,0}\delta_{i,1} , \\
\Delta B &= B(\tau_1) - B(\tau_0) , \\
\Delta\tau &= \tau_1 - \tau_0 .
\end{aligned}
\tag{3.47}
$$

3.5 Reflection and Emission from Ground Surfaces

The effect of the ground surface may be calculated using the interaction principle. The ground is treated as a layer with a transmission of unity, no source, and whatever reflection. The radiation emitted from the ground is the incident radiance on the lower

boundary. The internal radiance algorithm is used to calculate the downwelling radiance below the atmosphere (but above the ground)

$$
\begin{aligned}
I_a^+ &= \Gamma^+ I_a^{+\prime} \\
I_a^{+\prime} &= T_a^+ I_0^+ + R_a^+ I_g^- + S_a^+ \\
\Gamma^+ &= [1 - R_a^+ R_g]^{-1} .
\end{aligned}
\tag{3.48}
$$

where the a subscription refers to the total atmosphere layer, and g refers to the ground. The downwelling radiation from the atmosphere is what the radiation would be with no ground $I_a^{+\prime}$ multiplied by the multiple reflection factor Γ^+. The radiation upwelling from the top of the atmosphere is found from adding the atmosphere layer to the ground layer, namely

$$
\begin{aligned}
I_0^- &= R_T^- I_0^+ + T_T^- I_g^- + S_T^- \\
R_T^- &= R_a^- + T_a^- \Gamma^- R_g T_a^+ \\
T_T^- &= T_a^- \Gamma^- \\
S_T^- &= S_a^- + T_a^- \Gamma^- R_g S_a^+ \\
\Gamma^- &= [1 - R_g R_a^+]^{-1} .
\end{aligned}
\tag{3.49}
$$

3.5.1 Lambertian Surfaces

By definition a Lambertian surface emits and reflects equally in all directions. The reflected radiance is the ground albedo times the incident flux divided by pi. The reflected radiation is assumed to be unpolarized. The matrix operator for a Lambertian surface is

$$
|R_g|_{jj'ii'} = 2A_g w_{j'} \mu_{j'} \delta_{m,0} \delta_{i,1} ,
\tag{3.50}
$$

where A_g is the ground albedo ($A_g = 1 - \epsilon_g$ where ϵ_g is the ground emissivity).

The thermal radiation emitted by a Lambertian surface is unpolarized and isotropic

$$
|I_g^-|_{ji} = (1 - A_g) B(T) \delta_{m,0} \delta_{i,1} .
\tag{3.51}
$$

3.5.2 Fresnel Surfaces

A flat dielectric surface behaves according to the Fresnel reflection formulae. The incident radiation is reflected specularly such that the incident zenith angle equals the reflected zenith angle. The perpendicular or horizontal polarization is reflected differently than the parallel or vertical polarization. The Fresnel reflection formulae for a vacuum/dielectric interface are

$$R_V(\mu) = \frac{m^2\mu - \sqrt{m^2 + \mu^2 - 1}}{m^2\mu + \sqrt{m^2 + \mu^2 - 1}}$$
$$R_H(\mu) = \frac{\mu - \sqrt{m^2 + \mu^2 - 1}}{\mu + \sqrt{m^2 + \mu^2 - 1}} \,, \tag{3.52}$$

where μ is the cosine of the incident zenith angle and m is the complex index of refraction of the dielectric surface. These reflection coefficients are in general complex and are for the electric field amplitudes. Put in terms of the radiation intensity, the Stokes reflection matrix is

$$|R_g|_{jj'} = \begin{pmatrix} \frac{1}{2}(|R_V|^2 + |R_H|^2) & \frac{1}{2}(|R_V|^2 - |R_H|^2) & 0 & 0 \\ \frac{1}{2}(|R_V|^2 - |R_H|^2) & \frac{1}{2}(|R_V|^2 + |R_H|^2) & 0 & 0 \\ 0 & 0 & \mathrm{Re}(R_V R_H^*) & -\mathrm{Im}(R_V R_H^*) \\ 0 & 0 & \mathrm{Im}(R_V R_H^*) & \mathrm{Re}(R_V R_H^*) \end{pmatrix} \delta_{jj'} \,, \tag{3.53}$$

where the reflection coefficients are at the angles $\mu = \mu_{j'}$ (Tsang et al. 1985).

The thermal radiation emitted by a semi-infinite absorbing Fresnel surface is polarized and angle dependent

$$|I_g^-|_j = \begin{pmatrix} 1 - \frac{1}{2}(|R_v|^2 + |R_h|^2) \\ -\frac{1}{2}(|R_v|^2 - |R_h|^2) \\ 0 \\ 0 \end{pmatrix} B(T) \,. \tag{3.54}$$

3.6 The Radiative Transfer Model Algorithm

The radiative transfer algorithm is coded as a Fortran subroutine. The input parameters are the properties of the atmospheric layers, the boundary conditions, and control parameters. The output is the radiances at the discrete quadrature angles for each azimuthal Fourier mode. The atmospheric parameters specified for each layer are the layer

thickness, layer boundary temperatures, extinction, single scatter albedo, and Legendre series coefficients for the six unique elements of the scattering matrix. The boundary conditions for the top boundary are the solar direction and flux and incident blackbody radiation from space. For the bottom boundary they are ground surface temperature, surface type (Lambertian or Fresnel), and associated properties. For efficiency any number of boundary conditions may be applied to one atmosphere.

Because the azimuthal Fourier modes decouple, the doubling and adding of layers proceeds separately for each mode. The method developed here of calculating the azimuthal modes for the scattering matrix, however, provides all of the Fourier modes at once (via an FFT). For this reason the scattering matrices for all of the atmospheric layers are computed and stored before doubling and adding begins. The computation of the scattering matrix from the Legendre coefficients is optimized by using the symmetries described in section 3.3.3 ($\phi \to 2\pi - \phi$, $\mu \to -\mu$, and the packing of cosine and sine modes into one four vector). Another efficiency is that any number of Stokes parameters may be used (I; I,Q; I,Q,U; $,I,Q,U,V$), since some applications do not require all four Stokes parameters.

To assure that energy is conserved it is important that the scattering matrix be normalized. Since the quadrature integrations are exact for low enough powers of μ, normalization is achieved by using enough quadrature angles for the number of terms in the Legendre series. Before a scattering matrix for a layer is used the normalization is checked by summing the Stokes I-I element over all outgoing angles for each incident angle.

The atmospheric layers are processed from the top down. The scattering matrix for a layer is retrieved and the initial reflection and transmission matrices and source vectors are made for a specified small optical depth. The sources of diffuse radiation inside the medium may be thermal emission and/or scattered solar radiation. The doubling algorithm computes the reflection, transmission, and source for the full layer, and the layer is added to the rest of the atmosphere. The radiative transfer code assumes that all emitting species (gas and particles) are at the environmental temperature. A complete outline of the radiative transfer algorithm is given in appendix B.

3.7 Testing the Polarized Radiative Transfer Model

There are few polarized radiative transfer results in the atmospheric science literature which can be used for model testing. Most results are for specific applications and the descriptions do not contain enough details to simulate the results accurately. Also many of the polarized models are Monte-Carlo models which preclude high accuracy comparisons. Besides internal consistency checks, the present model has been tested in two ways. First, it has been operated in a scalar mode (no polarization) and compared with the radiative transfer model of Stamnes et al. (1988). The two models agree to high accuracy (better than 1 part in 10^5). Second, to test the polarization aspects of the model, comparisons were made with tables by Coulson, Dave, and Sekera (1960).

Coulson et al. contains tables of outgoing radiation from a conservative Rayleigh scattering layer. These tables list the upwelling and downwelling Stokes radiance vector (I, Q, U) as a function of angle for different optical depths, solar angles, and surface albedos. Comparisons were done for three cases of varying optical depth and solar angle. The radiative transfer model developed here was run with eight angles (out of the 16 angles in the tables) using the user defined quadrature scheme. The upwelling and downwelling radiances were compared at azimuth angles of 0, 90, and 180 degrees (U is zero at 0 and 180 degrees). The incident solar beam is normalized to a flux of pi. Table 3.1 compares the upwelling radiation for one case. Note: Coulson et al. define Q with a sign opposite to that used here. The results in this table show the characteristic decline in agreement at large zenith angles (small μ). Table 3.2 summarizes the radiative transfer comparison. It shows the average and maximum absolute difference between the Coulson et al. tables and the model results for the three cases. On average the results agree to a few places in the fourth decimal.

Table 3.1: Comparison of model output with results of Coulson et al. for a homogeneous Rayleigh atmosphere of optical depth of 1. The upwelling radiance as a function of $\mu = \cos\theta$ for an azimuth of 90 degrees is shown. The solar flux is normalized to π, the cosine of the solar zenith angle is 0.8, and the ground albedo is 0.25.

μ	Present Model			Coulson et al.		
	I	Q	U	I	Q	U
.0600	.39769	-.05121	.24707	.39887	.05099	.24758
.1600	.40860	-.03995	.23359	.40894	.03988	.23375
.2800	.40477	-.02767	.20914	.40482	.02766	.20918
.4000	.39384	-.01568	.18112	.39380	.01570	.18114
.6400	.37258	.00779	.12477	.37248	-.00774	.12476
.8400	.36158	.02686	.07591	.36147	-.02681	.07590
.9600	.35787	.03813	.03609	.35776	-.03808	.03609
1.0000	.35705	.04168	.00000	.35694	-.04181	.00000

Table 3.2: Summary of differences between radiative transfer model and tables by Coulson et al. The average and maximum absolute difference of the radiances over the eight upwelling zenith angles at azimuths of 0, 90, and 180 degrees between the tables and model results for the three cases. The optical depth and cosine of the solar zenith angle are listed.

Optical Depth	Solar μ_0	Ground Albedo	Average Error			Maximum Error		
			I	Q	U	I	Q	U
1	0.8	0.25	.00021	.00009	.00007	.00130	.00027	.00051
1	0.2	0.25	.00021	.00013	.00002	.00160	.00100	.00018
0.1	0.1	0.25	.00041	.00021	.00003	.00175	.00108	.00011

Chapter 4

MICROWAVE RADIATIVE TRANSFER MODEL COMPARISON

Simple approximate radiative transfer models are often used in microwave radiative transfer studies. Models that simplify the scattering source integral (by a two stream approach, for example) are less complex and take much less computer time. This is important when modeling three-dimensional inhomogeneities or when speed is necessary for remote sensing retrievals. The question arises as to the accuracy of these simple models. The highly accurate radiative transfer model developed here can be used to check a simple model, albeit only in the plane-parallel domain.

The simple model chosen for comparison is Eddington's second approximation which has been used extensively by Weinman (Weinman and Davies 1978, Wu and Weinman 1984, Kummerow and Weinman 1988) and others. In this model the Eddington two-stream model is solved first. From the Eddington fluxes the scattering source term is derived. The radiative transfer equation is then simply integrated over optical depth at the desired observation angle. The two polarizations (horizontal and vertical) are treated separately with no interaction. To facilitate detailed comparisons a version of this Eddington model was programmed for the comparison. The method and results are presented in detail in this chapter to facilitate future duplication of results for checking of microwave radiative transfer computer codes.

4.1 Eddington Model

The appropriate radiative transfer equation for passive microwave applications is plane-parallel, azimuthally symmetric with only thermal sources.

$$\mu \frac{dI}{d\tau} = -I + \frac{\tilde{\omega}}{2} \int_{-1}^{+1} P(\mu,\mu')I(\mu')d\mu' + (1 - \tilde{\omega})T , \qquad (4.1)$$

where I is the radiation intensity expressed in brightness temperature, P is the phase function, $\tilde{\omega}$ is the single-scatter albedo, and T is the environment temperature. In this case polarization is not included, so the radiance is a scalar rather than a vector.

The Eddington approximation expands the radiance field to first order in the cosine of the zenith angle ($I = I_0 + I_1\mu$). Using the notation of Meador and Weaver (1980) the radiance field may be expressed as a function of the upward and downward fluxes (I^+ and I^-)

$$I(\pm\mu) = \frac{1}{2}\left[(2 \pm 3\mu)I^+ + (2 \mp 3\mu)I^-\right] \ . \tag{4.2}$$

The phase function is also expanded to first order

$$P(\Theta) = 1 + 3g\cos\Theta = 1 + 3g\mu\mu' \ , \tag{4.3}$$

where g is the asymmetry parameter. Substituting these forms for the radiance and phase function and integrating over μ from 0 to 1 gives

$$\pm\frac{dI^\pm}{d\tau} = -\left(1 \pm \frac{3}{4}\right)I^+ - \left(1 \mp \frac{3}{4}\right)I^- + \tilde{\omega}\left[(I^+ + I^-) \pm \frac{3}{4}g\left(I^+ - I^-\right)\right] + (1-\tilde{\omega})T \ , \tag{4.4}$$

which may be rearranged into a two-by-two matrix equation for the upward and downward fluxes:

$$\frac{d}{d\tau}\begin{pmatrix} I^+ \\ I^- \end{pmatrix} = \begin{pmatrix} -t & -r \\ r & t \end{pmatrix}\begin{pmatrix} I^+ \\ I^- \end{pmatrix} + \begin{pmatrix} +\beta \\ -\beta \end{pmatrix} \tag{4.5}$$

$$r = \left[1 - \tilde{\omega}(4 - 3g)\right]/4$$

$$t = \left[7 - \tilde{\omega}(4 + 3g)\right]/4$$

$$\beta = (1 - \tilde{\omega})T \ .$$

For a uniform layer, where the coefficients r and t are constant, the two-stream radiative transfer equation may be solved analytically to get solutions in terms of exponentials. The eigenvalues for the matrix operator are

$$\lambda = \pm\sqrt{t^2 - r^2} = \pm\sqrt{3(1 - \tilde{\omega})(1 - \tilde{\omega}g)} \tag{4.6}$$

and the eigenvectors are

$$\begin{pmatrix} -r \\ t + \lambda \end{pmatrix} \ , \quad \begin{pmatrix} t + \lambda \\ -r \end{pmatrix} \tag{4.7}$$

where λ is the positive eigenvalue. The homogenous solution, the solution for no source term, is then

$$
\begin{aligned}
I_h^+ &= -rC^+ e^{\lambda\tau} + (t+\lambda)C^- e^{-\lambda\tau} \\
I_h^- &= (t+\lambda)C^+ e^{\lambda\tau} - rC^- e^{-\lambda\tau} \;.
\end{aligned}
\tag{4.8}
$$

The full solution requires that the particular solution for the source term be added to the homogeneous solution. If the thermal source is linear in optical depth ($\beta = \beta_0 + \beta_1\tau$) then the particular solution is

$$
\begin{aligned}
I_p^+ &= -\frac{\beta_1}{\lambda^2} + \frac{(\beta_0 + \beta_1\tau)}{t+r} \\
I_p^- &= \frac{\beta_1}{\lambda^2} + \frac{(\beta_0 + \beta_1\tau)}{t+r} \;.
\end{aligned}
\tag{4.9}
$$

The constants C^+ and C^- may be derived from the boundary conditions, i.e. the fluxes incident on the layer. For multiple layers the boundary conditions of all the layers must be simultaneously satisfied. One convenient approach is to use the doubling and adding algorithms. For a two stream model the transmission and reflection are scalars instead of matrices, but the doubling and adding algorithms are identical. The initial transmission, reflection, and source coefficients for an infinitesimal layer of thickness $\delta\tau$ are

$$
T = 1 - t\delta\tau \;, \quad R = -r\delta\tau \;, \quad S = \beta\delta\tau \;.
\tag{4.10}
$$

For a given set of boundary conditions the radiances at the layer interfaces are calculated from the internal radiance equations (section 3.4.3). The boundary conditions are incident cosmic radiation at the top and surface emission and reflection at the bottom. For a Lambertian surface the emissivity is independent of angle and may be used directly for the two-stream reflectivity. For a Fresnel surface, however, the emissivity varies with angle and some averaged value must be used. The Fresnel emissivities are numerically averaged over the two polarizations and over angle (16 quadrature angles are used)

$$
\bar{\epsilon} = \int_0^1 [\epsilon_v(\mu) + \epsilon_h(\mu)]\,\mu d\mu \;.
\tag{4.11}
$$

The second part of this Eddington model is to use the internal Eddington fluxes to calculate the source term and integrate the radiative transfer equation. The source term has thermal emission and scattering components

$$J(\tau,\mu) = (1 - \tilde{\omega})T(\tau) + \frac{\tilde{\omega}}{2}\int_{-1}^{+1} P(\mu,\mu')I_{edd}(\mu')d\mu' \ . \tag{4.12}$$

In terms of the Eddington fluxes I^+ and I^- for a layer the source term is

$$J(\tau,\mu) = \beta_0 + \beta_1\tau + \tilde{\omega}\left(I^+ + I^-\right) + \frac{3}{2}\tilde{\omega}g\mu\left(I^+ - I^-\right) \ , \tag{4.13}$$

which has the form

$$J(\tau) = B_0 + B_1 + D^+e^{\lambda\tau} + D^-e^{-\lambda\tau} \ . \tag{4.14}$$

The downwelling radiation at the surface is due to the cosmic radiation and the integral of the source term:

$$I^+(\tau^*,\mu) = T_c\exp\left(-\tau^*/\mu\right) + \frac{1}{\mu}\int_0^{\tau^*} J(\tau,\mu)\exp\left(-(\tau^* - \tau)/\mu\right)d\tau \ , \tag{4.15}$$

where τ^* is the optical depth at the bottom of the atmosphere. The upwelling radiation at the top of the atmosphere is from the surface emission, reflection of the downwelling radiation, and the integral of the source term:

$$I^-(0,\mu) = \left[\epsilon(\mu)T_g + (1 - \epsilon(\mu))I^+(\tau^*,\mu)\right]\exp\left(-\tau^*/\mu\right)$$

$$+ \frac{1}{\mu}\int_{\tau^*}^0 J(\tau,-\mu)\exp\left(-\tau/\mu\right)d\tau \ . \tag{4.16}$$

For a Fresnel surface the emissivity ϵ depends on polarization, and this is the only polarization dependence in this model. The simple form of the source term $J(\tau,\mu)$ allows the integrals to be done analytically for each layer, and the results for each layer are then summed.

4.2 Precipitation Modeling Comparison

The multi-stream model and the Eddington model were compared by modeling the microwave radiative transfer through a simple precipitating atmosphere. The comparison was done to determine the accuracy of the Eddington model specifically in microwave

Table 4.1: Atmospheric parameters for model comparison

Height (km)	Temperature (°K)	Rel. Hum. (%)	Cloud LWC (g/m³)	Gaseous Extinction (km⁻¹) 19 GHz	37 GHz	85 GHz
15	205	0	0	.00045	.00106	.00166
8	247	100	0.1	.01698	.04263	.12222
4	273	100	0	.02775	.03325	.13149
0	299	80				

Table 4.2: Some Mie calculation results for model comparison

Frequency (GHz)	Type	Temperature (C)	Rain rate (mm/hr)	Extinction (km⁻¹)	Albedo	Asymmetry
19.35	Ice	−15	2	.0005873	.8233	.0338
19.35	Rain	+15	2	.03299	.0918	−.0171
85.5	Ice	−15	50	3.222	.9872	.5347
85.5	Rain	+15	50	5.060	.5127	.3060

precipitation retrieval applications, rather than in a general radiative transfer sense. The tests were performed at three microwave frequencies in remote sensing use today: 19.35, 37.0, and 85.5 GHz. The atmosphere contained a four km thick rain layer and a four km thick ice and cloud layer. The atmospheric parameters of the layers and the corresponding gaseous (and cloud water) absorption for the three frequencies is given in Table 4.1. The rain and ice layers had the same Marshall-Palmer size distribution from 0.06 to 3.00 mm diameter hydrometeors. Three Marshall-Palmer rain rates (2, 10, 50 mm/hr) that cover a wide range of conditions were used. Results of some of the Mie scattering calculations for the rain and ice layers are given in Table 4.2. Simulations were also done with a cloud layer containing no ice hydrometeors. Two ground types were modeled: a Lambertian land surface having an emissivity of 0.90 and a Fresnel water surface, both at a temperature of 299°K. The water surface had a complex index of refraction of (7.004, −2.595) at 19 GHz, (5.408, −2.801) at 37 GHz, and (3.689, −2.187) at 85 GHz. The cosmic blackbody radiation of 2.7°K was incident from above. The multi-stream radiative transfer model used eight Lobatto quadrature angles, and the Eddington model was evaluated at the same angles.

The upwelling brightness temperatures from the multi-stream model and the brightness temperature differences between the two models is given in two tables. Table 4.3 is for the land surface, which has no polarization, and Table 4.4 is for the water surface. Results are listed for nadir and at about 49 degrees zenith angle (cosine=.65239). Figure 4.1 summarizes the brightness temperature difference results. In general, Eddington's second approximation reproduces the upwelling brightness temperatures from the multi-stream polarization model quite well. The simple model, however, has significant errors at intermediate optical depths (near unity). This is to be expected from the Eddington model. At small optical depths the two-stream calculation is nearly irrelevant because there is little scattering. At large optical depths, where there is much scattering, the radiative transfer is near the diffusion regime which the two-stream Eddington model can duplicate. At optical depths near one, the brightness temperature differences have a wide range, from -1.5 to $-8.5°K$. To put these differences in terms of retrieved rain rate, the rain rate can be adjusted in the multi-stream model (leaving all other parameters unchanged) until the brightness temperature is the same as the Eddington model. For example, for the 37 GHz case with 10 mm/hr rain rate, ice layer, and land surface the Eddington model output at nadir look angle corresponds to a rain rate of 8 mm/hr. For the 37 GHz, 2 mm/hr rain rate case the Eddington model predicts a warmer brightness temperature than zero rain or ice produces. The brightness temperature difference graph also shows the warm bias to the Eddington model. The warm bias means that the Eddington model would systematically underestimate the precipitation for scattering based retrieval methods.
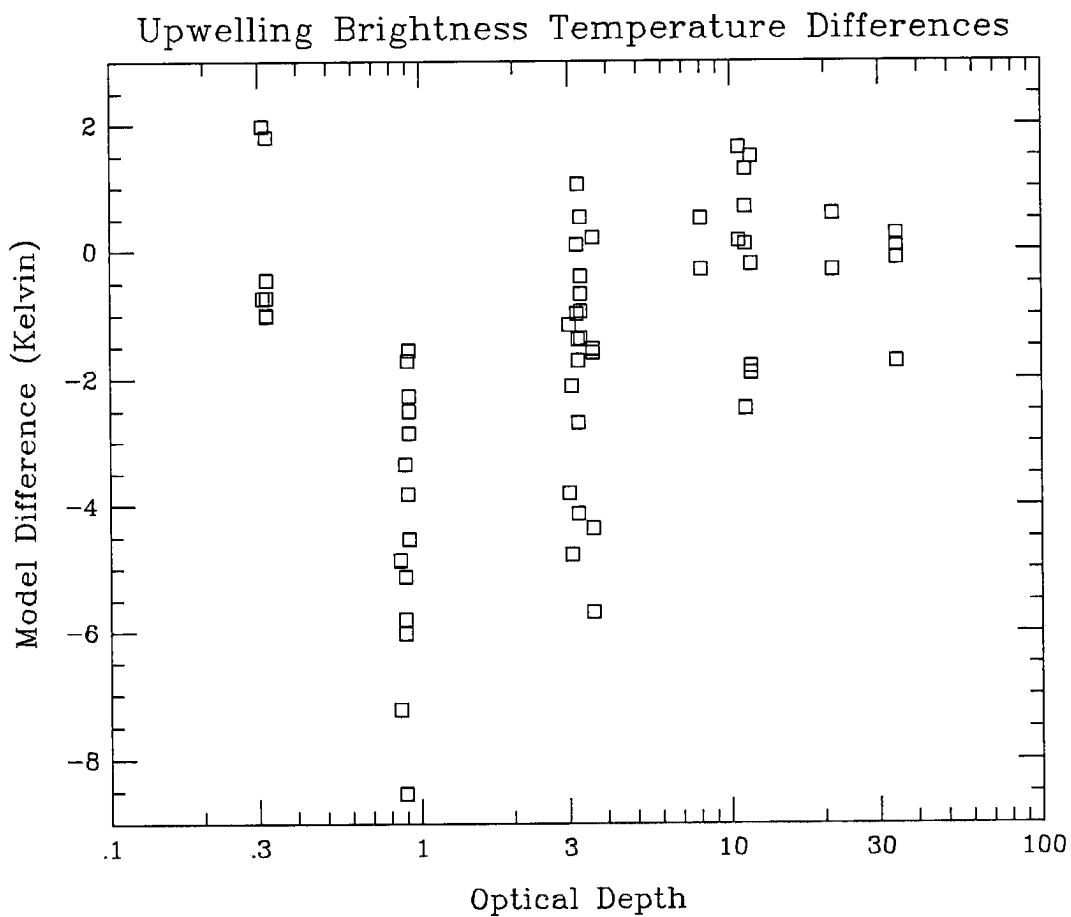
Figure 4.1: Upwelling brightness temperature difference between models as a function of optical depth. The difference is the multi-stream model minus the Eddington model. All cases described in the text are plotted. Results are shown for the three frequencies, the three rain rates, both land surfaces, and the two viewing angles.

Table 4.3: Radiative transfer model comparison results for a land surface. The upwelling brightness temperature from the multi-stream model and the difference (multi-stream − Eddington) between the two models at two zenith angles is tabulated. Simulations were performed for three frequencies and three Marshall-Palmer rain rates (R.R.).

Freq (GHz)	R.R. (mm/hr)	Brightness Temp I(49°)	I(0°)	T_B Difference I(49°)	I(0°)	Optical depth
Rain and ice layers
19	2	278.14	279.08	−.99	1.81	.32
19	10	274.95	278.92	−4.53	−2.27	.92
19	50	257.20	264.39	−.40	−1.36	3.28
37	2	269.25	274.21	−8.53	−6.02	.89
37	10	242.05	252.31	−1.38	−4.13	3.22
37	50	189.41	208.30	−.21	−1.80	11.67
85	2	242.93	255.53	−1.53	−5.68	3.60
85	10	190.94	211.74	.69	−2.47	11.15
85	50	138.70	158.83	.07	−1.73	34.15
Rain layer only
19	2	278.46	279.28	−.74	1.98	.31
19	10	277.39	280.54	−3.82	−1.71	.91
19	50	268.30	271.96	.10	−.98	3.20
37	2	272.44	276.32	−7.22	−4.86	.86
37	10	260.87	265.12	−1.16	−3.81	3.01
37	50	253.68	256.32	1.63	.16	10.65
85	2	263.94	268.84	−2.11	−4.78	3.07
85	10	260.66	264.11	.51	−.30	8.05
85	50	259.48	262.38	.58	−.31	21.27

Table 4.4: Radiative transfer model comparison results for a water surface. The upwelling brightness temperature from the multi-stream model and the difference (multi-stream − Eddington) between the two models at two zenith angles is tabulated. Vertical and horizontal polarizations are shown for 49 degrees; polarizations are the same at nadir. Model results are with both a rain layer and an ice layer.

Freq (GHz)	R.R. (mm/hr)	Brightness Temp			T_B Difference		
		V(49°)	H(49°)	(0°)	V(49°)	H(49°)	(0°)
19	2	234.70	203.82	193.89	−.45	−1.01	−.73
19	10	267.16	260.60	250.19	−1.55	−2.85	−2.50
19	50	257.76	256.56	263.93	.53	−.67	−.94
37	2	261.17	252.25	244.39	−3.34	−5.80	−5.12
37	10	243.31	240.55	251.66	1.05	−1.71	−2.69
37	50	191.11	187.71	208.30	1.49	−1.91	−1.80
85	2	243.74	241.94	255.13	.21	−1.59	−4.36
85	10	191.53	190.35	211.74	1.29	.11	−2.46
85	50	138.89	138.51	158.83	.26	−.12	−1.73

Chapter 5

PRECIPITATION INVERTIBILITY STUDY

Since the late 1970's there has been a gradual increase in the sophistication of modeling microwave radiative transfer through precipitating atmospheres. During this time there has been a corresponding realization of the complexities of accurate precipitation retrieval using passive microwave sensors. Wilheit et al. (1977) use a simple unpolarized radiative transfer model to calculate upwelling 19 GHz radiation from a uniform rain layer over the ocean. There is no ice hydrometeors and the thickness of the rain layer is fixed by the freezing level. These numerous assumptions lead to a simple brightness temperature-rain rate relationship showing an increase in T_B with rain rate up to a saturation point. Huang and Liou (1983), using a more sophisticated radiative transfer model with polarization, simulate upwelling radiation at 19, 37, and 85 GHz from a precipitating atmosphere with variable thickness rain and ice layers. Their modeling of the horizontal and vertical brightness temperature over land and water shows how a rain layer depolarizes the radiation from the ocean and how scattering from an ice layer greatly depresses the brightness temperature at 85 GHz. Wu and Weinman (1984) develop a simple approximate polarized radiative transfer model to study the effects of non-spherical ice hydrometeors, showing that these ice particles can lead to significant polarization effects. Kummerow (Kummerow 1987, Kummerow and Weinman 1988) investigates the effects of a horizontally finite geometry in a precipitating atmosphere. This model has rain and ice layers with oblate spheroidal ice particles. The modeling results demonstrate the large errors introduced in observing precipitating systems with sensor resolutions much larger than the natural horizontal scale. This three dimensional modeling effort, although using a simplified radiative transfer model, indicates the extent to which the plane-parallel

geometry is an approximation. Recent work by Mugnai and Smith (Mugnai and Smith 1988, Smith and Mugnai 1988, Mugnai et al. 1990) uses numerical cloud models to derive realistic vertical distributions of water and ice hydrometeors for plane-parallel microwave radiative transfer modeling. They emphasize the importance of the vertical distribution of cloud liquid water in precipitation retrieval. Their use of weighting functions allows a detailed examination of the effects of cloud microphysics on the upwelling microwave radiation and demonstrates the necessity of having multiple frequencies to characterize the precipitating system.

As the more recent research has shown, the upwelling microwave brightness temperatures from a precipitating atmosphere vary significantly with many microphysical parameters, such as cloud liquid water, the concentration, size, and vertical distribution of liquid and solid hydrometeors, etc. Given the multi-dimensional nature of the relevant precipitation parameters and the wide range of parameters observed in real precipitating systems, it would seem necessary to have many independent measurements to character- ize the precipitation accurately. For passive microwave observations these independent measurements would be brightness temperatures measured at different frequencies, po- larization states, or observation angles. Having several independent measurements does not mean, however, that the desired atmospheric parameters can be uniquely determined. The passive microwave observation of a precipitating atmosphere may be thought of as a multi-dimensional non-linear function: the function domain is a vector of atmospheric parameters and the function range is the measured (or modeled) brightness temperatures. The function is the transfer of microwave radiation through a precipitating atmosphere, while the inverse of the function represents the microwave precipitation retrieval prob- lem. If the function is multi-valued, i.e. a vector of brightness temperatures corresponds to more than one vector of atmospheric parameters, then retrieval is impossible. The purpose of the research described in this chapter is to explore the form of the forward function, specifically its degree of multi-valuedness, rather than to invent a particular retrieval scheme.

By choosing a relatively small number of the most important precipitation parameters and making some simplifying assumptions about the precipitation structure it is possible

to model the forward radiative transfer function numerically. The microwave radiative transfer model described in chapters 2 and 3 was used to calculate the polarized brightness temperatures at a number of microwave frequencies for many (1800) atmospheric states. A very simple two-layer precipitation structure was assumed. Seven parameters were varied in the radiative transfer modeling: layer thickness and Marshall-Palmer rain rate for the rain and ice layers, cloud liquid water content, temperature lapse rate, and surface emissivity. The atmospheric variables were varied to completely explore the parameter space rather than to give a statistical representation of actual precipitation events. The radiative transfer results were analyzed by tabulating the number of atmospheric states (input vectors) that gave virtually identical brightness temperatures (output vectors).

5.1 Radiative Transfer Modeling

The simple precipitating atmosphere structure used for the radiative transfer modeling consisted of four layers. In increasing height there was a rain layer, a rain and cloud layer, an ice and cloud layer, and a clear layer. The boundary between the rain and ice was fixed at the freezing level, and the cloud layer extended to one-half kilometer below the freezing level. The ice layer thickness and the total rain thickness were parameters that varied in the model. The top of the clear layer was at 15 km with a temperature of 205. The temperature of the layers depended on the uniform lapse rate. The relative humidity was specified at the layer interfaces (section 2.1) and was fixed. The distribution of liquid and ice hydrometeors was vertically homogenous. Table 5.1 shows the atmospheric structure and the parameter values used in the modeling.

The seven model parameters determining the atmospheric state were varied over a wide range of values. The rain layer thickness was varied in four steps from 1 km to 4 km, while the ice layer thickness was varied from 0 to 4 km, also in four steps. The rain layer had five values of Marshall-Palmer rain rate, from 2 to 40 mm/hr. The Marshall-Palmer "rain" rate for the ice layer was set to either 30% below, the same as, or 50% above that of the rain layer. There were three values of cloud liquid water and of temperature lapse rate. The surface emissivity was treated separately for the land and water cases.

Table 5.1: Structure of precipitation model and values of parameters varied. z_r and z_i are the thicknesses of the rain and ice layer respectively. R_r and R_i are the Marshall-Palmer rain rates for the rain and ice layers. ℓ is the cloud liquid water content. γ is the temperature lapse rate. ϵ is the land surface emissivity.

level	height (km)		temp (°K)	R.H. (%)	LWC (g/m^3)
1	15	_____	205	0	
		moist air			0
2	$z_r + z_i$	_____	$273 - \gamma z_i$	100	
		ice and cloud			ℓ
3	z_r	_____	273	100	
		rain and cloud			ℓ
4	$z_r - 0.5$	_____	$273 + \gamma 0.5$	100	
		rain			0
5	0	_____	$273 + \gamma z_r$	80	

$z_r = 1, 2, 3, 4$ km	$z_i = 0, 1, 2, 4$ km
$R_r = 2, 5, 10, 20, 40$ mm/hr	$R_i = -30, 0, +50\%$ of R_r
$\ell = 0.25, 0.5, 1.0$ g/m^2	$\gamma = 5.0, 6.5, 8.0$ C/km
Land: $\epsilon = 0.85, 0.90, 0.95$	Water: $\epsilon = 1.00, 1.10$ of $\epsilon_{fresnel}$

The three emissivities (0.85, 0.90, and 0.95) used for land were assumed independent of frequency. Two emissivities were used for water surfaces: the Fresnel value, and 1.10 times the Fresnel value. The model parameters were varied independently of each other, so there were 1800 different atmospheric states, or 5400 land cases and 3600 water cases.

The scattering properties of the hydrometeors was calculated from Mie theory assuming a Marshall-Palmer distribution (section 2.2). The scattering results depend on the particle temperature through the index of refraction. The temperature of the particles was set to that of the average environmental temperature of the layer, rounded to the nearest 5 C. The maximum diameter in the truncated Marshall-Palmer distribution was 3 mm and there were 50 integration steps in the Mie calculation. Liebe's millimeter wave propagation code was used to calculate the absorption due to oxygen, water vapor, and cloud liquid water (section 2.1). The 2.7°K cosmic blackbody radiation was included.

The radiative transfer model, the microwave gaseous absorption, and Mie scattering programs described above were combined with a control program to make the program

that ran all of the cases. The upwelling and downwelling polarized brightness temperatures (I and Q) were computed at six gaussian quadrature angles per hemisphere. For each atmospheric state the radiative transfer was calculated for seven frequencies: 6.0, 10.7, 19.35, 22.235, 37.0, 85.5, and 157.0 GHz.

5.2 Model Output Analysis Method

The radiative transfer modeling run produced polarized brightness temperatures at six upwelling angles for seven frequencies for 9000 distinct cases of atmospheric and surface properties. For the analysis only the I and Q brightness temperatures at 54 degrees zenith angle and the difference between the I brightness temperatures at 11 and 83 degrees zenith angle ($\Delta I = I(11) - I(83)$) was utilized. This effectively gives three "observables" for each frequency (total brightness temperature, degree of polarization, and angular variation of brightness temperature) for a total of 21 for each case. The model output can be thought of as 9000 discrete points in a function that operates on a seven dimensional atmospheric/surface state vector to produce an output vector of up to 21 brightness temperatures.

The analysis attempted to measure the multi-valuedness of the precipitation–microwave radiation function from the model output. The analysis method went through all output brightness temperature vectors and for each one determined how many output vectors were close to it (see figure 5.1). Two vectors were considered close if one fell within a multi-dimensional box of specified size around the other (i.e. the brightness temperature difference in all dimensions was less than the specified amount). For example, a brightness temperature box size of one Kelvin means that a multi-dimensional box with sides two Kelvin long is constructed around each point. The total number of pairs of vectors that were close was determined, and statistics were accumulated on the difference between the atmospheric states of those close pairs. The difference between the atmospheric states of cases that have close output brightness temperatures is an indication of the degree of multi-valuedness. There is less problem performing a precipitation retrieval if similar brightness temperatures correspond to similar atmospheric parameters than if they correspond to much different parameters. For each atmospheric or surface parameter the

number of differences and the average difference were tabulated for all the close pairs of

output vectors. For the 5400 land cases, for example, there are over 14 million pairs, and

for a particular analysis there might be 2000 pairs that are judged to be close. Of those

there might be only a few hundred that have different rain rates, because most of the

differences were in the other parameters.

Microwave Brightness
Temperature Space

T_{85}

T_{37}

T_{19}

ℓ

Precipitation
Parameter Space

Z_r

R_r
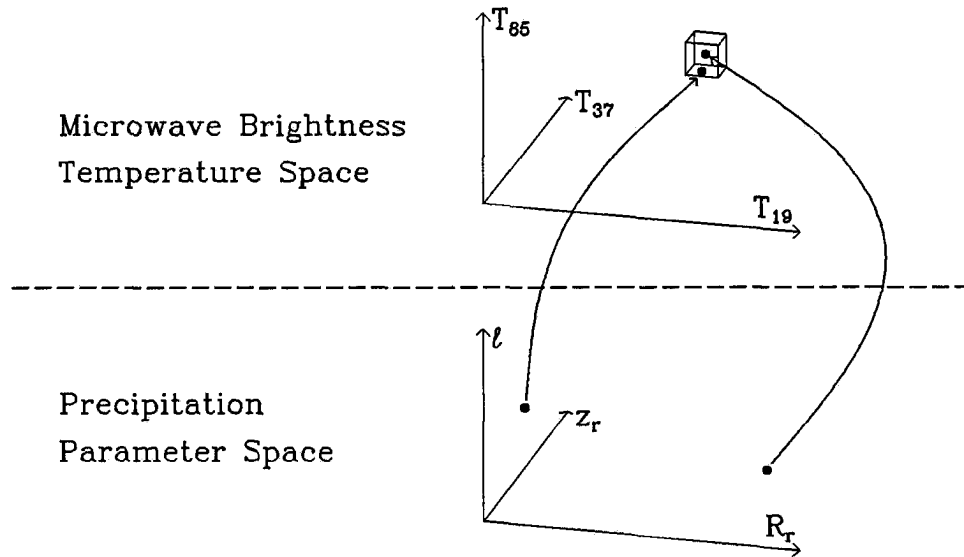
Figure 5.1: Schematic drawing of the analysis method. The microwave–precipitation
function relates points in precipitation parameter space to points in microwave brightness
temperature space. If two separate points in precipitation parameter space are within ΔT_b
of each other then the function is not invertible at that point. The analysis method uses
the total number of pairs of points that are close (within the T_b box) as a measure of the
uniqueness and accuracy of microwave precipitation retrieval.

Many analyses were performed with different numbers of brightness temperatures

in the output vector and different size boxes for the closeness criterion. The bright-

ness temperature box size corresponds (to some degree) to the accuracy of measurement

and modeling, in that two points are indistinguishable if they are closer than the errors.

From probability considerations it would be expected that the larger the distance cutoff

(greater the measurement error) the more close pairs would be found (the less unique

the retrieval would be). Different combinations of model output brightness temperatures

(i.e. different frequencies and polarizations) were used in the analyses. It is expected that

the greater the number of independent "measurements" or vector dimensions the more

accurate and unique the retrievals would be. By adjusting the number of brightness temperatures used, the number of frequencies needed for a reasonably unique retrieval can be determined. The importance of different frequencies and polarizations on retrievals of the various atmospheric parameters can be determined by performing analyses with different combinations of brightness temperatures. The analysis can be performed by selecting any combination of frequencies, and using brightness temperature combinations: I; I,Q; $I,Q,\Delta I$; V; V,H; or $V,H,\Delta I$ ($V = I + Q$ and $H = I - Q$). The land and water cases were analyzed separately.

5.3 Results of Analysis

Figure 5.2 shows how the brightness temperature close pair fraction (f) increases with increasing distance criterion (box size) for land and water surface cases with all seven of the frequencies used. Multi-valuedness increases greatly with uncertainty in brightness temperature. The slope of the plot of $\log f$ vs. $\log \Delta T_B$ is a measure of the dimensionality of the brightness temperature space. Taking the higher points (to avoid sampling problems), the slope for the land cases is 3.75 and for water cases is 2.98. This measure of dimension is considerably less than the topological dimension of seven for the land cases and fourteen for the water cases because the frequencies are not entirely independent of each other. The measured dimensions also show that the radiative transfer process has lost some of the information in the seven dimensional atmospheric parameter space. Table 5.2 gives the detailed results of the T_B box size analysis.

How the fraction of close pairs of brightness temperatures varies with the number of frequencies is shown in figure 5.3. The degree of multi-valuedness increases dramatically with fewer frequencies, from a close pair fraction of 10^{-5} with all seven frequencies to 10^{-1} for one frequency. The water surface cases are less multi-valued than the land cases for the same frequencies, due to the additional polarization information and the advantageous radiometrically cold surface. The graph shows a wide range in the number of close pairs for a given number of frequencies. This indicates that the uniqueness of the retrieval depends on the particular set of frequencies measured as well as the number of frequencies.
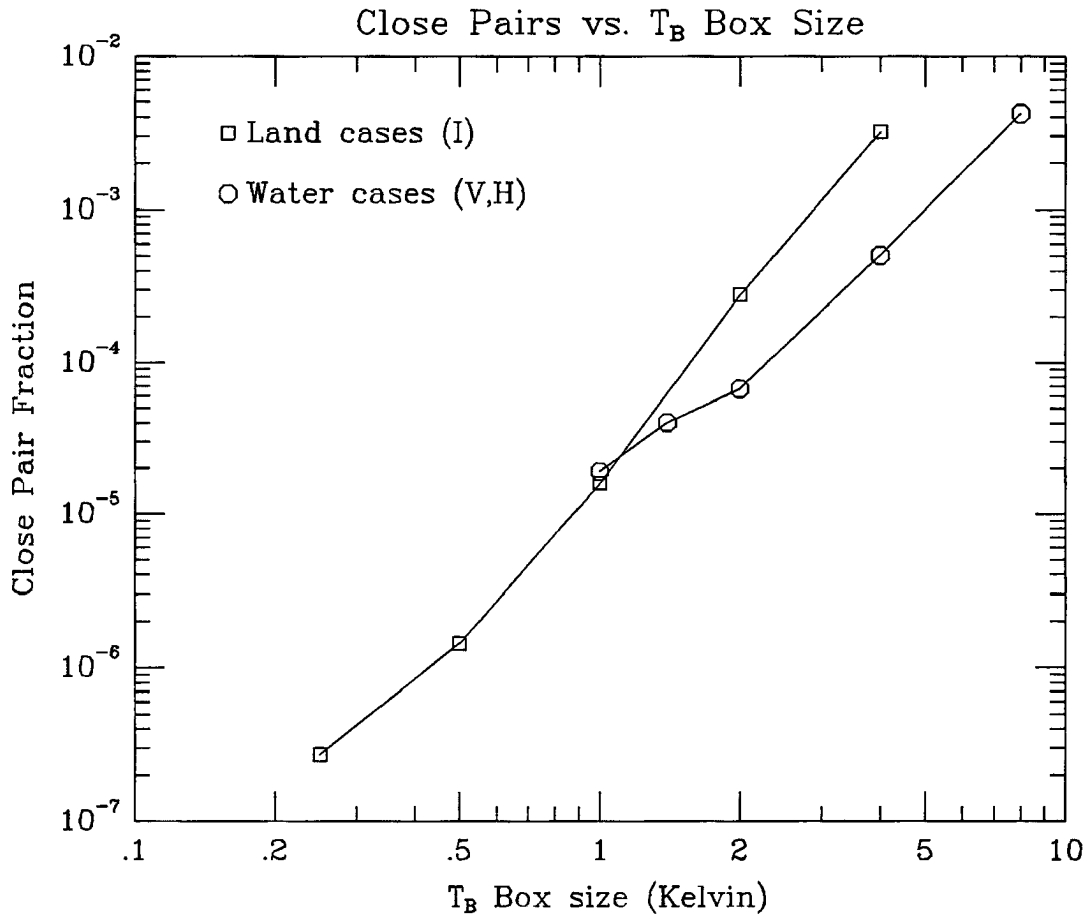
Figure 5.2: Close brightness temperature pair fraction versus brightness temperature distance criterion. Land and water surface analyses with all seven frequencies are shown.
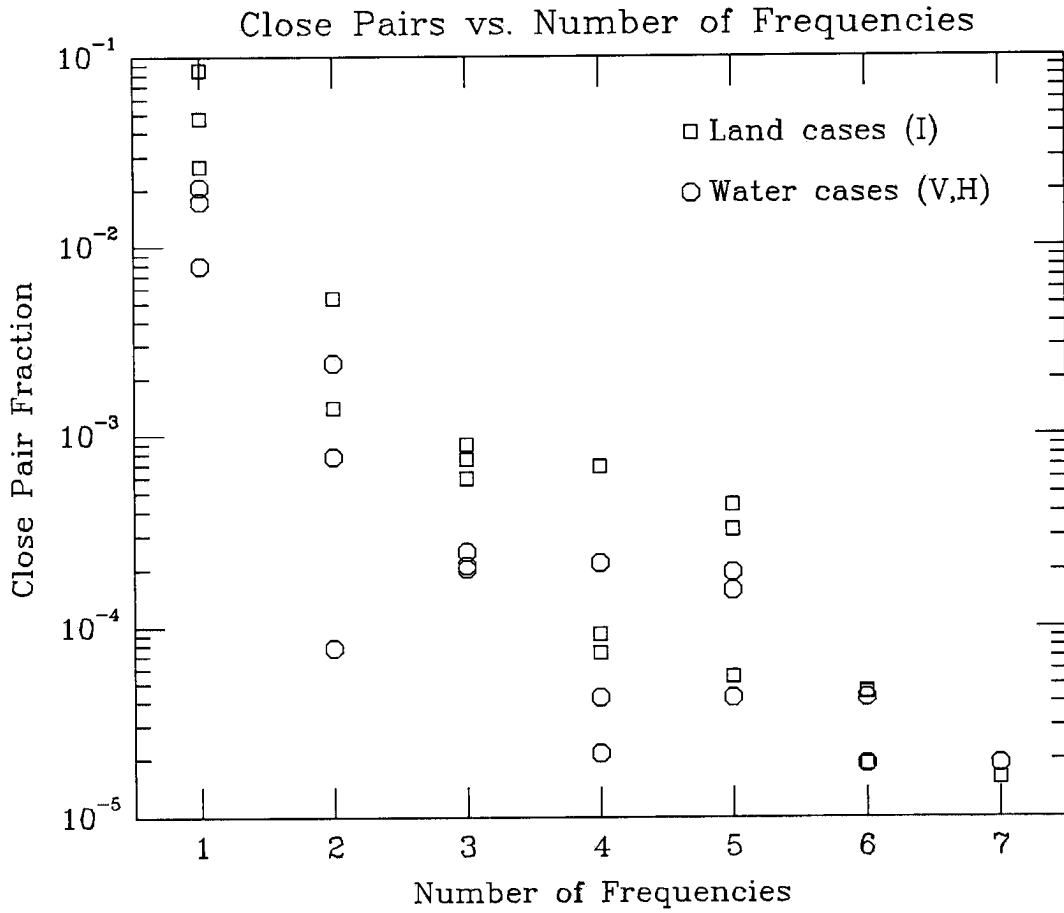
Figure 5.3: Close brightness temperature pair fraction versus number of frequencies. The brightness temperature distance criterion is 1.0°K.

The detailed results of the multiple frequency analyses are given in tables 5.3 through 5.6. These results are all from analyses with a brightness temperature distance criterion of 1.0°K. Tables 5.3 and 5.4 give the close pair fraction for the land and water surface cases respectively. They also contain, for each atmospheric parameter, the fraction of the close pairs that have a difference in that parameter. The atmospheric cases that have close brightness temperatures must, by design, have some difference in their parameters, but may have several parameters (rain rate, cloud LWC, etc.) that are the same. Thus of all the close pairs in an analysis, only some fraction will have a difference in a particular precipitation parameter. For certain applications only the number of cases with a difference in a particular parameter (e.g. rain rate) is relevant; this can be found by multiplying the parameter fraction by the close pair fraction. The second set of tables (5.5 and 5.6) have different information for the same analyses, again separated into land and water cases. These tables contain the number of close pairs and the average difference in the atmospheric parameters. As described in the analysis methods section, a histogram of the differences in the atmospheric parameters is accumulated for the close pairs. The average difference in a parameter is the mean value of the parameter calculated from this histogram. All of the tables are sorted according to the close pair fraction.

The results clearly show the importance of utilizing multiple frequencies for precipitation retrieval. Low frequencies (6 and 10 GHz) are crucial to an unique retrieval because of their ability to penetrate through the precipitation to the surface. Combinations of frequencies which include a low frequency have a smaller close pair fraction even than combinations which have more frequencies but are without a low frequency (e.g. 6,19,37,85 GHz with $f_{pair} = 9.25 \times 10^{-5}$ vs. 19,22,37,85,157 GHz with $f_{pair} = 4.35 \times 10^{-4}$ over land). For water surfaces a combination of 10 and 85 GHz with both V and H polarizations does remarkably well for only two frequencies. The highest frequency (157 GHz) does not markedly reduced the multi-valuedness of the precipitation retrieval. Combinations with frequencies further apart do better (e.g. 22 GHz is nearly redundant with 19 GHz), confirming the notion that the brightness temperatures become more independent as the frequencies separate. Single frequencies are very poor at uniquely determining the atmospheric state.

Polarization information is relevant only over water surfaces. The upwelling brightness temperatures over land are nearly unpolarized, so using Q as well as I in the analysis gives the same close pair fraction. Over a water surface, which is radiometrically cold and highly polarized, the polarization information can be important. When using many frequencies the addition of the H channel to the V channel does not add much new information, but with just one frequency the additional channel can be highly significant (e.g. at 19 GHz $f_{pair} = 7.90 \times 10^{-3}$ for V, H polarizations vs. $f_{pair} = 4.82 \times 10^{-2}$ for V alone). A few of the analyses looked at using information about the angular variation of the upwelling radiation in the form of ΔI described above. Comparing the close pair fraction for the same combination of frequencies with and without ΔI shows that the angular information is fairly significant to the retrieval process. It is likely, however, that the utility of the angular structure of the radiation determined under plane-parallel assumptions would be masked by the inhomogeneities in many real precipitation fields.

As would be expected the average difference in the parameters generally increases with the close pair fraction. This means that the atmospheric parameters of cases that result in similar brightness temperatures are further apart as the precipitation function becomes more multi-valued. For analyses with many frequencies the average difference in the rain rate, ice amount, and layer thicknesses is small compared to the range of variation, indicating that most of the close pairs had precipitation parameters that were similar. Over a water surface when many frequencies were used the temperature lapse rate was the source of most of the multi-valuedness with the other parameters having few or no differences. The analysis with 19, 37, and 85 GHz and the angular variation parameter ΔI shows an interesting result. Most of the multi-valuedness came from the surface emissivity parameter, so for the other parameters the degree of multi-valuedness was down near that for the analysis with all seven frequencies. By comparing analyses done with and without a particular frequency the precipitation parameters most dependent on that frequency can be found. The surface properties are most keenly sensed by the 6 GHz frequency. The 157 GHz frequency is only useful for sensing the overlay ice layer. The higher frequencies are important for retrieving cloud liquid water. These frequency-parameter relationships

are simply what would be expected from the known interactions of microwave radiation with precipitating atmospheres.

Interpretation of these results should be tempered by acknowledging the shortcomings of the modeling. Since only a small number of atmospheric parameters could be varied the precipitation structure had to be very simple. There was little vertical structure in the model, just two homogeneous precipitating layers. The hydrometeors were solid spheres with a simple Marshall-Palmer size distribution. The freezing level determined the boundary between the rain and ice layers. The assumptions caused there to be couplings between different physical parameters, e.g. surface temperature and rain layer thickness, cloud water path and ice layer thickness, etc. The plane-parallel nature of the model avoided the issues of horizontal inhomogeneities and different footprint resolutions of the frequencies. The accuracy of determining the multi-valuedness of the precipitation function was hindered by the coarseness of the discretization of the precipitation parameters. Even though the modeling, by necessity, had many simplifying assumptions, enough of the important parameters were varied to learn something about the precipitation retrieval function. If a retrieval is multi-valued with such a simple precipitation model then it is likely to be even more multi-valued in a real situation unless other constraining information is applied.

Table 5.2: Precipitation invertibility analysis results showing effect of changing the distance criterion. The number of close brightness temperature pairs and corresponding fraction of all pairs is given. All seven frequencies were used in the analysis of 5400 land and 3600 water cases. For each atmospheric parameter the fraction of the close pairs that have a difference in the parameter is tabulated. z_r and z_i are the thicknesses (km) of the rain and ice layer respectively . R_r and R_i are the Marshall-Palmer rain rates (mm/hr) for the rain and ice layers. ℓ is the cloud liquid water content (g/m^3). γ is the temperature lapse rate (°K/km). ϵ is the surface emissivity factor.

T_B's	Sfc	ΔT_B	N_{pair}	f_{pair}	(z_r)	(R_r)	(z_i)	(R_i)	(ℓ)	(γ)	(ϵ)
I	L	.25	4	2.74×10^{-7}	.00	1.00	.00	.00	.00	.00	.00
I	L	.50	21	1.44×10^{-6}	.00	.90	.10	.10	.00	.05	.00
I	L	1.00	233	1.60×10^{-5}	.23	.49	.48	.62	.22	.33	.00
I	L	2.00	4099	2.81×10^{-4}	.26	.42	.46	.72	.30	.59	.03
I	L	4.00	46995	3.22×10^{-3}	.49	.54	.53	.78	.41	.70	.22
V,H	W	.50	0	0	.00	.00	.00	.00	.00	.00	.00
V,H	W	1.00	123	8.44×10^{-6}	.00	.00	.01	.01	.01	.99	.00
V,H	W	1.40	261	1.79×10^{-5}	.00	.00	.02	.08	.02	.98	.00
V,H	W	2.00	437	3.00×10^{-5}	.00	.00	.09	.19	.04	.94	.00
V,H	W	4.00	3269	2.24×10^{-4}	.10	.14	.28	.52	.11	.79	.00
V,H	W	8.00	27117	1.86×10^{-3}	.44	.44	.48	.75	.32	.70	.03

Table 5.3: Precipitation invertibility analysis results showing effect of different frequency combinations. The fraction of brightness temperature pairs that are within the 1.0°K distance criterion is shown. For each atmospheric parameter the fraction of the close pairs that have a difference in the parameter is tabulated (parameters labeled as in table 5.2). Only land surface cases are included.

Frequencies	T_B's	f_{pair}	(z_r)	(R_r)	(z_i)	(R_i)	(ℓ)	(γ)	(ϵ)
6,10,19,22,37,85,157	$I, \Delta I$	3.36×10^{-6}	.02	.98	.00	.00	.00	.02	.00
6,10,19,22,37,85,157	I, Q	1.60×10^{-5}	.23	.49	.48	.62	.22	.33	.00
6,10,19,22,37,85,157	I	1.60×10^{-5}	.23	.49	.48	.62	.22	.33	.00
6,10,19,37,85,157	I	1.89×10^{-5}	.26	.43	.50	.63	.24	.35	.00
10,19,22,37,85,157	I	4.50×10^{-5}	.64	.28	.25	.38	.11	.31	.55
6,10,19,22,37,85	I	4.56×10^{-5}	.25	.28	.52	.73	.49	.37	.00
6,10,19,37,85	I	5.47×10^{-5}	.27	.26	.54	.72	.50	.39	.00
6,19,37,85	I	7.36×10^{-5}	.32	.34	.50	.70	.47	.41	.08
6,10,85,157	I	9.25×10^{-5}	.30	.64	.44	.68	.29	.41	.08
19,37,85	$I, \Delta I$	1.34×10^{-4}	.21	.10	.01	.04	.02	.11	.92
6,10,19,22,37	I	3.26×10^{-4}	.16	.27	.61	.76	.48	.27	.01
19,22,37,85,157	I	4.35×10^{-4}	.61	.15	.09	.19	.03	.23	.76
6,19,37	I	5.97×10^{-4}	.29	.45	.66	.80	.57	.39	.12
19,22,37,85	I	6.88×10^{-4}	.58	.21	.21	.34	.14	.43	.69
10,19,37	I	7.48×10^{-4}	.39	.46	.64	.77	.53	.52	.26
19,37,85	I, Q	9.01×10^{-4}	.62	.28	.29	.44	.22	.47	.70
19,37,85	I	9.02×10^{-4}	.62	.28	.29	.44	.22	.47	.70
10,85	I	1.40×10^{-3}	.63	.66	.56	.81	.61	.63	.57
37,85	I	5.33×10^{-3}	.71	.43	.40	.59	.36	.56	.68
19,37	I	5.34×10^{-3}	.62	.57	.63	.77	.56	.62	.64
85	I	2.66×10^{-2}	.75	.65	.55	.79	.60	.64	.67
37	I	4.77×10^{-2}	.74	.64	.69	.82	.64	.66	.67
19	I	8.56×10^{-2}	.67	.76	.70	.90	.66	.66	.65

Table 5.4: Precipitation invertibility analysis results showing effect of different frequency combinations. The fraction of brightness temperature pairs that are within the 1.0°K distance criterion is shown. For each atmospheric parameter the fraction of the close pairs that have a difference in the parameter is tabulated (parameters labeled as in table 5.2). Only water surface cases are included.

Frequencies	T_B's	f_{pair}	(z_r)	(R_r)	(z_i)	(R_i)	(ℓ)	(γ)	(ϵ)
6,10,19,22,37,85,157	$V,H,\Delta I$	5.69×10^{-6}	.00	.00	.00	.00	.00	1.00	.00
6,10,19,22,37,85,157	V,H	8.44×10^{-6}	.00	.00	.01	.01	.01	.99	.00
10,19,22,37,85,157	V,H	8.44×10^{-6}	.00	.00	.01	.01	.01	.99	.00
6,10,19,37,85,157	V,H	8.44×10^{-6}	.00	.00	.01	.01	.01	.99	.00
6,10,19,22,37,85,157	V	9.33×10^{-6}	.00	.00	.06	.06	.06	.94	.00
6,10,85,157	V,H	9.54×10^{-6}	.04	.00	.09	.12	.10	.91	.00
6,10,19,22,37,85	V,H	1.88×10^{-5}	.00	.00	.08	.11	.07	.93	.00
6,10,19,37,85	V,H	1.88×10^{-5}	.00	.00	.08	.11	.07	.93	.00
6,19,37,85	V,H	1.89×10^{-5}	.00	.00	.08	.11	.07	.93	.00
19,37,85	$V,H,\Delta I$	2.97×10^{-5}	.00	.00	.00	.00	.00	.42	.62
10,85	V,H	3.46×10^{-5}	.20	.28	.37	.47	.29	.81	.05
19,22,37,85,157	V,H	6.96×10^{-5}	.35	.02	.01	.03	.00	.20	.70
6,10,19,22,37	V,H	8.68×10^{-5}	.00	.00	.31	.67	.11	.42	.00
6,19,37	V,H	8.98×10^{-5}	.01	.01	.33	.68	.14	.43	.00
10,19,37	V,H	9.35×10^{-5}	.02	.02	.32	.66	.13	.44	.01
19,22,37,85	V,H	9.67×10^{-5}	.33	.05	.04	.09	.02	.40	.59
19,37,85	V,H	1.10×10^{-4}	.35	.09	.07	.16	.04	.46	.58
19,37,85	V	2.29×10^{-4}	.49	.25	.27	.42	.21	.56	.54
19,37	V,H	3.43×10^{-4}	.34	.21	.35	.54	.24	.52	.41
37,85	V,H	1.07×10^{-3}	.65	.32	.27	.43	.18	.53	.54
19,37	V	1.28×10^{-3}	.55	.52	.58	.76	.52	.63	.48
37,85	V	2.23×10^{-3}	.68	.50	.43	.63	.39	.58	.52
19	V,H	3.51×10^{-3}	.49	.42	.60	.79	.61	.64	.45
37	V,H	7.71×10^{-3}	.71	.60	.61	.78	.54	.65	.50
85	V,H	9.19×10^{-3}	.75	.65	.53	.77	.54	.64	.51
85	V	1.19×10^{-2}	.75	.66	.55	.79	.60	.64	.51
19	V	2.14×10^{-2}	.64	.73	.67	.90	.65	.66	.49
37	V	2.35×10^{-2}	.73	.70	.69	.85	.63	.66	.50

Table 5.5: Precipitation invertibility analysis results showing effect of different frequency combinations. The number of brightness temperature pairs that are within the 1.0°K distance criterion is shown. The average of the difference in atmospheric parameters over the close pairs is tabulated (parameters labeled as in table 5.2). Only land surface cases are included.

Frequencies	T_B's	N_{pair}	$\overline{\delta z_r}$	$\overline{\delta R_r}$	$\overline{\delta z_i}$	$\overline{\delta R_i}$	$\overline{\delta \ell}$	$\overline{\delta \gamma}$	$\overline{\delta \epsilon}$
6,10,19,22,37,85,157	$I, \Delta I$	49	1.00	3.7	.00	.0	.00	1.50	.000
6,10,19,22,37,85,157	I, Q	233	1.00	3.8	1.19	2.5	.39	1.90	.000
6,10,19,22,37,85,157	I	233	1.00	3.8	1.19	2.5	.39	1.90	.000
6,10,19,37,85,157	I	276	1.00	3.8	1.19	2.4	.41	1.93	.000
10,19,22,37,85,157	I	656	1.05	5.9	1.29	3.2	.41	1.75	.066
6,10,19,22,37,85	I	665	1.00	4.5	1.26	3.5	.40	1.92	.050
6,10,19,37,85	I	797	1.00	4.5	1.28	3.4	.41	1.95	.050
6,19,37,85	I	1073	1.17	6.9	1.38	4.4	.43	1.93	.053
6,10,85,157	I	1348	1.18	7.2	1.50	5.8	.43	2.01	.050
19,37,85	$I, \Delta I$	1959	1.05	5.5	1.00	2.3	.44	1.58	.063
6,10,19,22,37	I	4746	1.03	6.0	1.40	4.7	.41	1.97	.050
19,22,37,85,157	I	6347	1.17	9.7	1.53	4.0	.43	1.74	.066
6,19,37	I	8697	1.21	10.9	1.65	7.3	.46	2.02	.053
19,22,37,85	I	10026	1.18	10.4	1.60	5.9	.45	1.77	.066
10,19,37	I	10897	1.14	10.4	1.75	7.4	.46	1.92	.062
19,37,85	I, Q	13136	1.22	10.8	1.73	6.3	.46	1.83	.066
19,37,85	I	13148	1.22	10.9	1.74	6.4	.46	1.83	.066
10,85	I	20369	1.41	12.5	1.81	11.0	.50	1.96	.061
37,85	I	77717	1.53	9.3	1.80	6.9	.48	1.90	.066
19,37	I	77864	1.32	13.4	1.96	10.5	.49	1.96	.065
85	I	387789	1.64	12.5	1.78	10.8	.51	1.97	.067
37	I	695414	1.64	11.5	1.96	9.3	.50	2.00	.067
19	I	1247290	1.46	17.6	2.03	16.7	.50	1.99	.065

Table 5.6: Precipitation invertibility analysis results showing effect of different frequency combinations. The number of brightness temperature pairs that are within the 1.0°K distance criterion is shown. The average of the difference in atmospheric parameters over the close pairs is tabulated (parameters labeled as in table 5.2). Only water surface cases are included.

Frequencies	T_B's	N_{pair}	$\overline{\delta z_r}$	$\overline{\delta R_r}$	$\overline{\delta z_i}$	$\overline{\delta R_i}$	$\overline{\delta \ell}$	$\overline{\delta \gamma}$	$\overline{\delta \epsilon}$
6,10,19,22,37,85,157	$V, H, \Delta I$	83	.00	.0	.00	.0	.00	1.50	.000
6,10,19,22,37,85,157	V, H	123	.00	.0	1.00	2.0	.25	1.50	.000
10,19,22,37,85,157	V, H	123	.00	.0	1.00	2.0	.25	1.50	.000
6,10,19,37,85,157	V, H	123	.00	.0	1.00	2.0	.25	1.50	.000
6,10,19,22,37,85,157	V	136	.00	.0	1.00	2.0	.25	1.50	.000
6,10,85,157	V, H	139	1.00	.0	1.00	1.7	.25	1.56	.000
6,10,19,22,37,85	V, H	274	.00	.0	1.00	2.7	.25	1.50	.000
6,10,19,37,85	V, H	274	.00	.0	1.00	2.7	.25	1.50	.000
6,19,37,85	V, H	275	1.00	3.0	1.04	2.8	.25	1.51	.000
19,37,85	$V, H, \Delta I$	433	1.00	3.0	1.00	4.0	.25	1.50	.100
10,85	V, H	504	1.17	8.5	1.60	6.3	.38	1.68	.100
19,22,37,85,157	V, H	1014	1.05	16.0	1.63	7.0	.25	1.54	.100
6,10,19,22,37	V, H	1266	.00	.0	1.05	3.7	.29	1.50	.000
6,19,37	V, H	1309	1.06	15.2	1.09	4.2	.31	1.52	.100
10,19,37	V, H	1363	1.00	6.6	1.15	4.1	.30	1.54	.100
19,22,37,85	V, H	1409	1.04	17.8	1.24	7.6	.29	1.58	.100
19,37,85	V, H	1609	1.05	16.5	1.53	7.3	.36	1.72	.100
19,37,85	V	3335	1.16	11.3	1.64	7.1	.45	1.81	.100
19,37	V, H	5000	1.06	15.7	1.56	10.3	.39	1.83	.100
37,85	V, H	15557	1.46	12.6	1.85	7.9	.44	1.87	.100
19,37	V	18685	1.22	13.4	1.86	10.5	.48	1.94	.100
37,85	V	32531	1.49	11.0	1.79	8.4	.49	1.90	.100
19	V, H	51200	1.20	17.7	1.83	15.4	.50	1.96	.100
37	V, H	112327	1.55	14.3	1.88	11.5	.47	2.00	.100
85	V, H	133998	1.63	12.7	1.79	10.9	.49	1.97	.100
85	V	172785	1.65	12.5	1.77	10.8	.51	1.97	.100
19	V	312344	1.37	19.1	2.04	18.6	.51	1.99	.100
37	V	341936	1.60	12.2	1.97	10.3	.50	1.99	.100

Chapter 6

SUMMARY AND CONCLUSIONS

Precipitation is an important but ill-measured element of climate and the general circulation. The hydrological cycle, through the heat of phase changes, is a large component of the energy budget of the earth, but the distribution of precipitation is poorly known Progress in climate modeling will require an accurate global climatology of precipitation for verification of the parameterizations used for clouds and precipitation. As a result of the inadequate coverage and sampling problems of rain gauges and weather radars, satellite instruments offer the best possibility for a global precipitation dataset. Microwave sensors have a distinct advantage over visible and infrared instruments because microwave radiation penetrates clouds and interacts directly with the precipitation elements. Passive microwave radiometers with many frequency channels have been in earth orbit for over a decade, but there is still no widely accepted rainfall retrieval algorithm. This is due to the complicating effects of the many atmospheric parameters which modulate the upwelling microwave radiation. Recent theoretical radiative transfer modeling has indicated that using multiple microwave frequencies should improve precipitation retrieval accuracy.

The purpose of the present research has been to develop a highly accurate radiative transfer model and to use the model to explore the issue of multiple frequencies in microwave radiative transfer in precipitating atmospheres. The tasks that were performed in this research are:

1. The development and testing of a fully polarized plane-parallel radiative transfer model for general use in remote sensing.

2. A comparison of the complex model with an Eddington-type two-stream model for simple precipitating atmospheres.

3. An examination of the invertibility of the precipitating atmosphere–microwave brightness temperature function.

6.1 Summary of the Radiative Transfer Model

The radiative transfer model developed for this research was designed to be highly accurate for use in remote sensing. Besides thermal emission, solar radiation was included for testing purposes and for use in visible and near IR remote sensing projects. A full polarization formulation was needed for model testing with solar scattering and for accurate future computations with non-spherical particles. Fully polarized means that the completely general transformation of the polarization state upon scattering is calculated. A multi-stream discretization of the angular field was used to achieve high accuracy. The model was programmed to be efficient, maintainable, and reliable. It was tested by comparisons with a discrete ordinate unpolarized model and with the Rayleigh scattering tables of Coulson et al.

The model developed for this research is a monochromatic plane-parallel polarized radiative transfer model. The model can solve the radiative transfer equation for vertically inhomogeneous atmospheres with solar and thermal sources of radiation. The full angular distribution of the radiance field is calculated, by discrete streams in zenith angle and by a Fourier series in azimuth angle. The angles of the discrete streams are chosen by one of five numerical quadrature scheme: Gaussian, double-Gaussian, Lobatto, and two new schemes which allow angles to be chosen at will. The polarization state of the radiance is represented by the four Stokes parameters (I, Q, U, V), and only the appropriate number of Stokes parameters need be used for a given calculation. If the Rayleigh-Jeans approximation is invoked the radiances are expressed in brightness temperature, otherwise the radiances are in units of Watts/(meter^2 ster micron). For microwave radiative transfer the radiance is azimuthally symmetric, thermal emission is the only source of radiation, and the U and V Stokes parameters are zero. In the microwave region the radiance is often expressed as horizontal and vertical polarizations: $I_V = I + Q$, $I_H = I - Q$.

The version of the model described here assumes that the scattering particles have a plane of symmetry and are randomly oriented. In this case the polarized scattering

information is completely described by six functions of scattering angle. These functions are input to the model as Legendre series. Inside the model the bi-directional scattering information is contained in a scattering matrix. For each pair of zenith angles (incoming and outgoing) a four-by-four scattering matrix defines the transformation of the polarized radiance due to a single scattering.

The major difficulty in implementing a polarized radiative transfer model as compared to an unpolarized one is the calculation of the scattering matrix from the Legendre series scattering information. This difficulty arises from the necessity of rotating the frame of reference of the polarization. The Q and U Stokes parameters are defined in terms a reference plane. The scattering information input to the model has the scattering plane as the reference, whereas the radiative transfer model has the vertical axis as the reference. In both polarized and unpolarized radiative transfer models the multiple scattering computations are performed independently for each Fourier azimuth mode (this is a result of the scattering depending only on the difference between the incident and outgoing azimuth angles). In an unpolarized model the addition theorem of associated Legendre functions provides a direct way to calculate the scattering for an azimuthal mode from the Legendre series coefficients. The polarization rotation prevents this method from working. Some previous models have used complicated series to transform from the Legendre series to the scattering matrix for each azimuth mode.

For this research a simpler method of rotating the polarization was developed. The method is to rotate the polarization explicitly in physical space rather than in the Fourier space. For each pair of zenith angles (incident and outgoing) the Legendre series are summed and the polarizations rotated for a number of discrete azimuthal angle differences. This produces the four-by-four scattering matrix for each azimuth angle difference, which is then fast Fourier transformed to make the scattering matrices for all azimuth modes at once. Various symmetries of the scattering matrix are used to speed up the computation. Since all modes of the scattering matrix are computed at once, while the multiple scattering calculations are performed sequentially for each Fourier mode, the scattering matrices are pre-calculated and stored. As a result of the symmetries of the polarized scattering matrix,

even modes of I and Q couple only to the odd modes of U and V, so the radiance vector used in the model is $(I_{cos}, Q_{cos}, U_{sin}, V_{sin})$.

The doubling and adding technique is used to solve the radiative transfer equation. Each input layer is divided into a number of homogeneous sublayers with each sublayer being thin enough for the finite differencing to be accurate. Infinitesimal generator initialization is used to relate the scattering matrix to the reflection and transmission matrices. These matrices are a way of expressing the linear transformation of radiation incident on a layer to radiation emerging from the layer (the interaction principle). There may be thermal sources which are linear with optical depth, or the single scattering of solar radiation which is exponential with optical depth. The sublayers are integrated up to the full layer with the doubling algorithm. The reflection and transmission matrices, and source vectors for the layer are combined with the previous layers with the addition algorithm. The reflection and transmission matrices, and source vectors for the whole atmosphere are combined with the reflection and emission from the ground below and blackbody radiation from above to find the radiation upwelling from the top of the atmosphere and the radiation downwelling from the bottom. The surface reflection and emission may be either Lambertian or Fresnel (Fresnel is used for water surfaces in the microwave). Once the radiative properties of the atmosphere are found numerous boundary conditions may be applied at little additional cost.

To perform calculations of microwave brightness temperatures the radiative transfer model must be coupled with a gaseous absorption model and with scattering calculations from precipitation size particles. Liebe's millimeter wave propagation model was used to calculate the absorption coefficients of oxygen, water vapor, and cloud droplets (which are too small to scatter microwaves). The absorption depends on the pressure, temperature, humidity, and cloud liquid water content. In this research the scattering hydrometeors were assumed to be spherical and Mie theory was implemented. The four Mie functions of scattering angle were stored as Legendre series. Standard sources were used for the index of refraction of water and ice. The Mie calculations were done for a Marshall-Palmer (exponential) distribution of particle sizes, although a modified gamma distribution was implemented.

6.2 Summary of Model Comparisons

The complex radiative transfer model described above was compared with a simple model in use by the microwave remote sensing community. The purpose of the comparison was to determine the accuracy of the simple model and to find out if the gain in accuracy of the present model is worth the additional complexity and computer time. The simple model uses Eddington's second approximation. This involves solving the Eddington two-stream model first, and then integrating the radiative transfer equation over optical depth using the two-stream solution in the scattering source term. This model treats the two polarizations separately, and polarization is only introduced by a polarized (water) surface.

The comparisons were performed for microwave radiative transfer through very simple precipitating atmospheres. The system consisted of two homogeneous precipitating layers, one consisting of ice hydrometeors and cloud droplet and the other of raindrops, with the same Marshall-Palmer size distribution. Marshall-Palmer rain rates of 2, 10, and 50 mm/hr over both land and water surfaces were simulated. Three microwave frequencies in use today were considered (19, 37, and 85 GHz).

The difference between the output of the two models is as large 8.5°K (the 2 mm/hr case at 37 GHz). The brightness temperature differences are less than about 2°K for small ($\ll 1$) and large ($\gg 1$) optical depths, but are larger at optical depths near one. The Eddington model usually produced brightness temperatures warmer than the multi-stream model. In general, it is concluded that the Eddington model is accurate enough to be used successfully for some precipitation retrieval work. There is, however, significant error at optical depths near one, which is the regime that brightness temperatures are most sensitive to precipitation, below the saturation region. The warm bias of the Eddington model would lead to a systematic underestimation of precipitation for scattering based retrieval methods.

6.3 Summary of Precipitation Invertibility Study

Recent work in precipitation retrieval suggests that multiple frequencies will be necessary for accurate remote sensing of rainfall. How many and which frequencies will be

needed? Can precipitation be uniquely retrieved even with multiple frequencies? An answer to these questions was sought in a theoretical study using the radiative transfer model described above. For this study the transfer of microwaves through a precipitating atmosphere (the "forward" problem) was thought of as a multi-dimensional function. The input to the function is a vector of atmospheric parameters, while the output is a vector of the brightness temperatures at different frequencies. The inverse of this precipitation–microwave function is the precipitation retrieval problem. If the function is multi-valued, then an observation of brightness temperatures does not uniquely determine an atmospheric state. The purpose of the study was to explore the invertibility of this function, to find how its multi-valuedness changes with the set of frequencies in the output vector.

The precipitation–microwave function was investigated by calculating the upwelling brightness temperatures for many different atmospheric cases and then analyzing the results. The simple atmospheric structure consisted of two homogeneous precipitating layers (a rain layer and an ice layer). Seven parameters were varied in the radiative transfer modeling: layer thickness and the Marshall-Palmer rain rate for the two layers, cloud liquid water content, lapse rate of temperature, and surface emissivity. A total of 1800 different atmospheric states were modeled with 5400 cases over land and 3600 cases over water. The radiative transfer was calculated at seven frequencies (6, 10, 19, 22, 37, 85, and 157 GHz).

The large volume of model output was analyzed by calculating a measure of the multi-valuedness of the precipitation–microwave function. The analysis operated on the upwelling brightness temperatures at a zenith angle of 54 degrees, using I over land and V and H polarizations over water. For a particular analysis some subset of all of the brightness temperatures (frequencies and polarizations) was used. The analysis consisted of constructing a multi-dimensional box around each vector of brightness temperatures, and counting how many other model output vectors were inside the box. In other words, all of the pairs of brightness temperature vectors that were less than some distance apart were counted. The fraction of the total number of pairs that were within the distance criterion was called the close pair fraction. Statistics on the difference between the atmospheric

parameters of close pairs was also collected. A smaller close pair fraction means the precipitation–microwave function is less multi-valued and the precipitation retrieval would likely be more accurate.

Obviously, as the size of the brightness temperature box is increased there are more close pairs. Thus precipitation retrieval becomes much less reliable as the uncertainty in the brightness temperatures increases. The slope of the log-log plot of close pair fraction vs. T_B box size is a measure of the dimensionality of the brightness temperature space. When all seven frequencies were used the dimension was 3.75 for land cases and 3.0 for water cases. These relatively small dimensions indicate that the seven frequencies were not independent of each other and that some information about the seven dimensional atmospheric state had been lost.

As more frequencies were used the retrieval became much more unique. There was, however, a wide range in the close pair fraction even with the same number of frequencies. Combinations that have frequencies further apart are better. Water cases were less multi-valued than land cases because of polarization information and the cold background. Polarization was important over water only when a small number of frequencies were used. The analysis of water surface cases with 10 and 85 GHz and H and V polarizations had a remarkably low close pair fraction, lower than some analyses with five frequencies. Low frequencies (6 and 10 GHz) were very important for uniqueness in retrievals. Only the low frequencies actually sense the surface and lower parts of the precipitation structure. The results indicate that precipitation retrieval methods involving only one frequency would be very poor.

This research had a number of assumptions and limitations which should be mentioned. The treatment of the hydrometeors was simplified in terms of the size distribution and physical properties. The vertical structure of the precipitation was very simple, and the discretization of the atmospheric parameter space was severely limited. These limitations suggest that whether a given number of frequencies would be adequate in a real situation can't be determined. On the other hand, a retrieval that is inaccurate with such a simple precipitation model would be worse in actuality.

The precipitation invertibility study demonstrates that precipitation retrieval algorithms should use all the available information, both multi-frequency and polarization. We agree with Mugnai et al. (1990) about the importance of microwave instruments having multiple channels over a wide range of frequencies, especially covering the lower frequencies. Precipitation retrieval algorithms that incorporate multiple frequencies, like that of Kummerow et al. (1989), should continue to be developed. Given the upward trend in the frequencies of passive microwave instruments (driven by the desire for increased spatial resolution), these studies indicate the importance of theoretical modeling in the frequency selection process for future instruments.

REFERENCES

Abramowitz, M., I. A. Stegun, 1972: *Handbook of Mathematical Functions with Formulas, Graphs, and Mathematical Tables,* National Bureau of Standards, 1046 pp.

Arkin, P. A., 1979: The relationship between fractional coverage of high cloud and rainfall accumulations during GATE over the B-scale array. *Mon. Wea. Rev.,* **107,** 1382–1387.

Bohren, C. F., and D. R. Huffman, 1983: *Absorption and Scattering of Light by Small Particles,* John Wiley & Sons, 530 pp.

Chandrasekhar, S., 1960: *Radiative Transfer,* Dover, 393 pp.

Coulson, K. L., J. V. Dave, and Z. Sekera, 1960: *Tables Related to Radiation Emerging from a Planetary Atmosphere with Rayleigh Scattering,* Univ. of Califonia Press, 548 pp.

Dave, J. V., 1970: Intensity and polarization of the radiation emerging from a plane-parallel atmosphere containing monodispersed aersols. *Appl. Optics,* **9,** 2673–2684.

Grant, I. P. and G. E. Hunt, 1969: Discrete space theory of radiative transfer. *Proc. Roy. Soc. London,* **A313,** 183–197.

Hovenier, J. W., 1969: Symmetry relationships for scattering of polarized light in a slab of randomly oriented particles. *J. Atmos. Sci.,* **26,** 488–499.

Huang, R., and K-N. Liou, 1983: Polarized microwave radiation transfer in precipitating cloudy atmospheres: Applications to window frequencies. *J. Geophys. Res.,* **88,** 3885–3893.

Ishimaru, A., D. Lesselier, C. Yeh, 1984: Multiple scattering calculations for non-spherical particles based on the vector radiative transfer theory. *Radio Sci.,* **19,** 1356–1366.

Kummerow, C. D., 1987: *Microwave radiances from horizontally finite, vertically structured precipitating clouds.* Ph.D. dissertation, Univ. of Minnesota, Minneapolis, 146 pp.

Kummerow, C. D., R. A. Mack, and I. M. Hakkarinen, 1989: A self-consistency approach to improve microwave rainfall rate esimation from space. *J. Appl. Met.,* **28,** 869–884.

Kummerow, C. D., and J. A. Weinman, 1988: Determining microwave brightness temperatures from horizontally finite and vertically structured clouds. *J. Geophys. Res.*, **93**, 3720–3728.

Liebe, H. J., 1985: An updated model for millimeter wave propagation in moist air. *Radio Sci.*, **20**, 1069–1089.

Meador, W. E., and W. R. Weavor, 1980: Two stream approximations to radiative transfer in planetary atmospheres: A unified description of existing methods and a new improvement. *J. Atmos. Sci.*, **37**, 630–643.

Mugnai, A., and E. A. Smith, 1988: Radiative transfer to space through a precipitating cloud at multiple microwave frequencies. Part I: Model description. *J. Appl. Met.*, **27**, 1055–1073.

Mugnai, A., H. J. Cooper, E. A. Smith, and G. J. Tripoli, 1990: Simulation of microwave brightness temperature of an evolving hailstorm at SSM/I frequencies. *Bull. Am. Met. Soc.*, **71**, 2–13.

Njoku, E. G., 1982: Passive microwave remote sensing of the earth from space — A review. *Proc. IEEE*, **70**, 728–750.

Press, W. H., B. P. Flannery, S. A. Teukolsky, W. T. Vetterling, 1986: *Numerical Recipes: The Art of Scientific Computing*, Cambridge University Press, 818 pp.

Ray, P. S., 1972: Broadband complex refractive indices of ice and water. *Appl. Optics*, **11**, 1836–1843.

Simpson, J., R. F. Adler, and G. R. North, 1988: A proposed tropical rainfall measuring mission (TRMM) satellite. *Bull. Am. Met. Soc.*, **69**, 278–295.

Smith, E. A., and A. Mugnai, 1988: Radiative transfer to space through a precipitating cloud at multiple microwave frequencies. Part II: Results ans analysis *J. Appl. Met.*, **27**, 1074–1091.

Spencer, R. W., H. M. Goodman, and R. E. Hood, 1989: Precipitation retrieval over land and ocean with the SSM/I: Identification and characteristics of the scattering signal. *J. Atmos. Ocean Tech.*, **6**, 254–273.

Spencer, R. W., D. W. Martin, B. B. Hinton, and J. A. Weinman, 1983: Satellite microwave radiances correlated with radar rain rates over land. *Nature*, **304**, 141–143.

Stamnes, K., S-C. Tsay, W. Wiscombe and K. Jayaweera, 1988: Numerically stable algorithm for discrete-ordinate-method radiative transfer in multiple scattering and emitting layer media. *Appl. Optics*, **27**, 2502–2509.

Thiele, O. W., Ed., 1987: On requirements for a satellite mission to measure tropical rainfall. NASA Ref. Pub. 1183, 49 pp.

Tsang, L., J. A. Kong, and R. T. Shin, 1985: *Theory of Microwave Remote Sensing*, John Wiley & Sons, 613 pp.

van de Hulst, H. C., 1981: *Light scattering by small particles,* Dover, 470 pp.

Warren, S. G., 1984: Optical constants of ice from the ultraviolet to the microwave. *App. Optics,* **23,** 1206–1225.

Weinman, J. A., and R. Davies, 1978: Thermal microwave radiances from horizontally finite clouds of hydrometeors. *J. Geophys. Res.,* **83,** 3099–3107.

Wilheit, T. T., A. T. C. Chang, M. S. V. Rao, E. B. Rodgers, and J. S. Theon, 1977: A satellite technique for quantitatively mapping rainfall rates over the oceans. *J. Appl. Met.,* **16,** 551–560.

Wiscombe, W. J., 1976a: On initialization, error and flux conservation in the doubling method. *J. Quant. Spectosc. Radiat. Transfer,* **16,** 477–489.

Wiscombe, W. J., 1976b: Extension if the doubling method to inhomogeneous source. *J. Quant. Spectosc. Radiat. Transfer,* **16,** 637–658.

Wiscombe, W. J., 1980: Improved Mie scattering algorithms. *Appl. Optics,* **19,** 1505–1509.

Wu, R., and J. A. Weinman, 1984: Microwave radiances from precipitating clouds containing apherical ice, combined phase and liquid hydrometeors. *J. Geophys. Res.,* **89,** 7170–7178.

Appendix A

NUMERICAL QUADRATURE SCHEMES

Numerical quadrature provides a method of accurately performing integrations numerically. A quadrature scheme provides a set of abscissae (x_i) and weights (w_i) that are used to approximate an integral

$$\int_a^b f(x)dx \approx \sum_{i=1}^n w_i f(x_i) \tag{A.1}$$

For radiative transfer computations the integral to be approximated is the scattering integral over cosine of the zenith angle (μ). To check that radiation is being conserved an integral of the phase function over all outgoing directions is performed. The integrand of for this normalization check is a polynomial in μ, because the phase matrix is expressed as a Legendre series. Quadrature schemes are chosen to be optimal, in the sense of being able to exactly integrate polynomials up to a certain degree. There is a trade off between flexibility in choosing the abscissae (x_i) and the highest degree for which the quadrature sum will be exact (see table A.1). The radiative transfer program described in chapter 3 has the choice of five quadrature schemes: Gaussian, double Gaussian, Lobatto, and two schemes in which the user can choose the some or all of the angles.

A.1 Gaussian Quadrature

The great mathematician Gauss developed the theory of numerical quadrature. The most powerful scheme, in that it exactly integrates the highest degree polynomial possible for the number of terms in the sum, is called Gauss-Legendre or Gaussian quadrature. In this scheme the abscissae are not constrained by the user, but are provided by the method. For an n- point quadrature the abscissae are the zeros of the n'th Legendre polynomial,

and the weights are related to the slope of the polynomial at the corresponding zero. For integration limits of -1 to 1 the abscissae and weights are defined by

$$P_n(x_i) = 0 \quad w_i = \frac{2}{(1 - x_i^2)[P_n'(x_i)]^2} \ , \quad i = 1, 2, \ldots, n/2 \qquad (A.2)$$

(see Ambramowitz and Stegun, 1972 for quadrature formulae).

The algorithm the radiative transfer program uses for Gauss-Legendre quadrature is due to Rybicki (see Numerical Recipes, Press et al. 1986). The approximate location of the abscissae is found from

$$x_i = \cos[\pi(i - \tfrac{1}{4})/(n + \tfrac{1}{2})] \ , \qquad (A.3)$$

and the Newton's method is used to zero in on the root of the polynomial. The Legendre polynomials are found by upward recursion. Gaussian quadrature can exactly integrate polynomials up to degree $2n - 1$, which seems twice as high as might be expected. This can be explained by noting that since both the x_i and the w_i are free to be selected there are actually $2n$ variables to adjust. The integral of all odd powers is zero, and this forces the quadrature schemes to have abscissae symmetric around zero.

The limits of the scattering integral are $\mu = -1$ to $\mu = 1$, representing both the downward hemisphere $(-1 \to 0)$ and the upward hemisphere $(0 \to 1)$. In order to avoid an angle at $\mu = 0$, only even n are used in the Gaussian quadrature. This gives the same angles in each hemisphere, so that for 8 angles in a hemisphere $n = 16$, but only the 8 positive x_i are found. This formulation of Gaussian quadrature is exact for integrations over both hemispheres, but not for integrations over just one hemisphere (as in a hemispheric flux calculation).

A variation on the Gaussian scheme called double-Gaussian quadrature is used when accurate hemispheric fluxes are desired. For this scheme Gaussian quadrature is used but the integration limits are now 0 to 1. Thus for eight angles per hemisphere $n = 8$. The x_i are found by a linear transformation of the abscissae given above:

$$P_n(z_i) = 0 \quad w_i = \frac{1}{(1-z_i)^2[P_n'(z_i)]^2} \ , \quad i = 1, 2, \ldots, n$$

$$x_i = \tfrac{1}{2}(z_i + 1) \ . \qquad (A.4)$$

A.2 Lobatto Quadrature

Lobatto quadrature is similar to Gaussian quadrature except the limits of the integration are included among the abscissae. For radiative transfer this is convenient because one of the quadrature angles is pointing toward the zenith and another is pointing toward nadir. For an n-point quadrature the abscissae are the zeros of the derivative of the $(n-1)$'th Legendre polynomial, and the weights are a function of the value of the polynomial at the abscissae. For integration limits of -1 to 1 the abscissae and weights are defined by

$$P'_{n-1}(x_i) = 0 \quad w_i = \frac{2}{n(n-1)[P_{n-1}(x_i)]^2} \ , \quad i = 1, 2, \ldots, n/2 \ , \tag{A.5}$$

and the weights for the endpoint abscissae $x = \pm 1$ are $w = \frac{2}{n(n-1)}$.

The algorithm the program uses for Lobatto quadrature is a modification of the one used for Gaussian quadrature. The approximate location of the root is given by

$$x_i = \sin[\pi(i - \frac{1}{2})/(n + \frac{1}{2})] \tag{A.6}$$

for even n. Again the root is found by Newton's method. Lobatto quadrature can exactly integrate polynomials up to degree $2n - 3$.

A.3 User Specified Quadrature

One quadrature method developed for this research has the user select all of the abscissae. Being able to specify the angles is quite useful when comparing radiative transfer calculations with tabulated values, as some of the uncertainties of interpolation are avoided. The scheme used here is quite straightforward and probably not original. The weights are found by requiring the quadrature sum to be exact for integrating polynomials up to degree $n - 1$:

$$\int_{-1}^{1} x^l dx = \sum_{i=1}^{n} w_i x_i^l = \alpha_l \ , \quad l = 0, 1, \ldots, n - 1$$

$$\alpha_l = \begin{cases} \frac{2}{l+1} & l \text{ even} \\ 0 & l \text{ odd} \end{cases} \ . \tag{A.7}$$

Since the integral of the odd powers is zero, the system of equations may be expressed with less terms as

$$\sum_{i=1}^{n/2} w_i x_i^{2l} = \frac{1}{2l+1} \ , \qquad l = 0, 1, \ldots, n/2 - 1 \ . \tag{A.8}$$

This series of equations is equivalent to a matrix equation and can be solved for the vector of weights w_i. The matrix is a special type called Vandermonde which can be solved in order N^2 operations rather than the usual N^3 operations (see Press et al. 1986) This type of system is the same as that for polynomial interpolation.

For $n/2$ angles per hemisphere the quadrature scheme is exact for polynomials up to degree $n-1$, which is about half as powerful as Gaussian quadrature (something has to pay for the ability to select the abscissae). The user specified method is, unfortunately, limited by instability problems. Depending on the particular abscissae chosen the instability occurs when more than about ten quadrature angles per hemisphere are used in double precision computations. The instability is manifest by extremely large weights (the weights should be between 0 to 1). Vandermonde matrices are "notoriously ill-conditioned, by their very nature" (Numerical Recipes).

A.4 Extra-angle Quadrature

Another quadrature method developed for this research has the user select some extra angles to add to the rest of the abscissae which come from Gaussian quadrature. The weights associated with these extra angles are set to zero. Since the weights are zero, the radiative transfer computation is equivalent to that with plain Gaussian quadrature. The resulting radiances at the Gaussian quadrature angles are identical to the those from the plain Gaussian case, and the radiances at the extra angles are effectively interpolated. Remote sensing observations are often obtained at one or just a few angles, and it is convenient be able to produce model radiances at exactly these angles.

For simplicity consider the unpolarized case of radiative transfer with one extra angle. Since the weight for the extra angle is zero the last column of the scattering matrix has all zeros. The last row is not zero, but contains the amount of radiation single scattered

into the extra angle for each of the incident Gaussian quadrature angles. The matrix mathematics of adding and doubling preserve the zeros in the last column (except for the last row in the last column which would be non-zero in the transmission matrix). This form of the final reflection and transmission matrices indicates that the extra angles behave as test angles, in that they only participate in the calculation of the output radiation. In fact, any radiation incident along an extra angle does not participate in scattering. The extra quadrature angles make the matrices bigger and thereby increase the computer running time, which goes as the cube of the number of angles. Usually only one or two extra angles is needed and the increase in computer time is not severe.

Table A.1: The maximum degree polynomial for which the various numerical quadrature schemes are exact for N angles per hemisphere. N_e is the number of extra-angles.

Quadrature type	Maximum degree
Gauss-Legendre	$4N - 1$
Double Gauss	$2N - 1$
Lobatto	$4N - 3$
User specified	$2N - 1$
Extra-angle	$4(N - N_e) - 1$

Appendix B

OUTLINE OF RADIATIVE TRANSFER MODEL ALGORITHM

This appendix presents an outline of the model algorithm in order to illustrate how the equations and methods described in chapter 3 are put together into a structure that solves the radiative transfer equation. This outline will also aid in understanding the Fortran program. As described in section 3.6 the radiative transfer model is coded as a subroutine with input parameters of the properties of the atmosphere and the boundary conditions, and output parameters of the radiances emerging from the top and bottom of the atmosphere. As the outline proceeds, the relevant equation numbers from chapter 3 and the Fortran subroutine names are listed.

- Make quadrature abscissae and weights (appendix A).
  GAUSS_LEGENDRE_QUADRATURE, DOUBLE_GAUSS_QUADRATURE,
  LOBATTO_QUADRATURE, QUADRATURE_WEIGHTS.

- Go through all of the layers and get a list of the scattering files. If a layer has only gaseous absorption then there is no scattering file. Determine if a temporary file is needed for the scattering matrices.
  Then for each scattering file:

  - Read in scattering file, retrieving extinction, albedo, and the Legendre coefficients for the six unique phase matrix elements (3.15, 3.23). READ_SCAT_FILE.

  - Make the Fourier modes of the scattering matrix (the C in equation 3.36, but without $\tilde{\omega}$). SCATTERING.

    * Find how many of the six Legendre series need to be summed. Rayleigh and Mie scattering are subsets of the general case and don't require all six series to be summed. Also, if less than four Stokes parameters are being used then not all series are summed. NUMBER_SUMS.

    * Loop over outgoing quadrature angles, incoming quadrature angles, and + or − hemisphere. As equation 3.36 implies, there are four parts of the scattering matrix (e.g. C^{++} is forward scattering of downwelling radiation, C^{+-} is backward scattering of upwelling radiation). Due to symmetry, only two of the four parts of the scattering matrix need to be calculated directly.

* Loop over azimuth angle differences $\Delta\phi_k$ (3.24, 3.25). A symmetry is used so the only $N_\phi/2 + 1$ points are calculated. For each μ_j, $\mu_{j'}$, and $\Delta\phi_k$:

  · Calculate the scattering angle $(\cos\Theta)$ (3.10) and sum the needed Legendre series (3.23). SUM_LEGENDRE.

  · Calculate the polarization transformed scattering matrix (3.16, 3.11–3.14). Depending on the number of Stokes parameters, only some of the matrix elements are calculated. ROTATE_PHASE_MATRIX.

  · Use the scattering matrix symmetry $(\phi \to -\phi)$ to do two $\Delta\phi_k$ terms for the price of one. MATRIX_SYMMETRY.

* Perform a fast Fourier transform in $\Delta\phi$ for each element of scattering matrix (3.26). FOURIER_MATRIX.

* For each azimuth mode combine the cosine and sine terms of the scattering matrix into the packed form (3.29,3.31,3.27,3.28). COMBINE_PHASE_MODES.

* Store the scattering matrix for each azimuth mode either in memory or a temporary file. Only two out of the four parts of the scattering matrix are stored (C^{++} and C^{+-}).

− If there is a solar source then make the Fourier modes of the solar pseudo-source vector. As indicated in equation (3.5) the direct source vector is just the first column of the scattering matrix evaluated for the solar incidence angle. It is calculated by the same method described above for the scattering matrix, but there is only a sum over outgoing angles since the incident angle is fixed. The M_{i1} part of (3.33) is stored (the scalar constant is multiplied later). DIRECT_SCATTERING.

• Loop over azimuth modes m:

  − Loop over layers from the top down:

    * If the scattering file for this layer is a new one then retrieve the stored scattering matrix. Make the two parts of the scattering matrix that aren't stored (C^{--} from C^{++}, and C^{-+} from C^{+-}). If there is a solar source retrieve the direct source vector. GET_SCATTERING, SCATTER_SYMMETRY, GET_DIRECT.

    * Check the normalization of the scattering matrix by integrating the Stokes I-I term over all outgoing angles for each incident angle. The sum must equal one. The normalization check is performed only for the 0'th azimuth mode. CHECK_NORM.

    * Calculate the number of sub-layers (for doubling) based on the optical depth of the layer and the desired initial layer thickness. The number of sub-layers is a power of two. The initial sub-layer thickness Δz is also calculated.

    * If there is a solar source then initialize the solar source vector (3.33, 3.41). INITIAL_SOURCE.

    * If there is a thermal source then get the Planck function for the temperatures at the top and bottom of the layer (3.6,3.7). Initialize the thermal source vector (3.41). THERMAL_RADIANCE, PLANCK_FUNCTION, INITIAL_SOURCE.

* If the layer has no scattering compute the reflection and transmission matrices and thermal source vector for the whole layer (no doubling required) (3.47). NONSCATTER_LAYER.

* Otherwise initialize the local reflection and transmission matrix (3.41), and double the reflection and transmission matrices and thermal and/or solar sources (3.44, 3.45, 3.46). INITIALIZE, DOUBLING_INTEGRATION.

* Add the layer onto the bottom of the rest of the atmosphere to get the atmosphere reflection, transmission, and source (3.42). COMBINE_LAYERS.

— Loop over boundary conditions to apply to the whole atmosphere:

* Calculate the ground surface reflection matrix and emission source vector for either Lambertian or Fresnel surfaces (3.50–3.54). LAMBERT_REFLECT, LAMBERT_RADIANCE, FRESNEL_REFLECT, FRESNEL_RADIANCE.

* Produce a thermal radiance vector for the thermal radiance incident from above, if any (3.6, 3.7).

* Combine the whole atmosphere layer with the ground layer, and using the interaction principle compute the upwelling radiance from the top of the atmosphere and the downwelling radiance from the bottom of the atmosphere (3.49). GROUND_EFFECT.

• Integrate the outgoing radiances over the quadrature angles to find the upwelling and downwelling fluxes.